




## ARTICLE



# Oligomeric CHMP7 mediates three-way ER junctions and ER-mitochondria interactions

Qingzhu Chu<sup>1,5</sup>, Jingru Wang<sup>1,5</sup>, Yuanjiao Du<sup>1</sup>, Tiantian Zhou<sup>1</sup>, Anbing Shi<sup>1,2</sup>, Juan Xiong<sup>3</sup> , Wei-Ke Ji<sup>1,2</sup>  and Lin Deng<sup>4</sup> 

© The Author(s), under exclusive licence to ADMC Associazione Differenziamento e Morte Cellulare 2022

In metazoans the endoplasmic reticulum (ER) undergoes extensive remodeling during the cell cycle. The endosomal sorting complexes required for transport (ESCRT) protein CHMP7 coordinates ESCRT-III dependent nuclear envelope reformation during mitotic exit. However, potential roles of ER-associated CHMP7 at non-mitotic stages remain unclear. Here we discovered a new role of CHMP7 in mediating three-way ER and ER-mitochondrial membrane contact sites (MCSs). We showed that CHMP7 localizes to multiple cellular membranes including the ER, mitochondrial-associated membranes (MAMs) and the outer mitochondrial membrane (OMM) via its N-terminal membrane-binding domain. CHMP7 undergoes dynamic assembly at three-way ER junctions and ER-mitochondrial MCSs through hydrophobic interactions among  $\alpha$  helix-1 and  $\alpha$  helix-2 of the C-terminal CHMP-like domain, which was required for tethering different organelles in vivo. Furthermore, CHMP7 mediates the formation of three-way ER junctions in parallel with Atlastins (ATLs). Importantly, CHMP7 also regulates ER-mitochondrial interactions and its depletion affects mitochondrial division independently of ESCRT complex. Taken together, our results suggest a direct role of CHMP7 in the formation of the ER contacts in interphase.

*Cell Death & Differentiation* (2023) 30:94–110; <https://doi.org/10.1038/s41418-022-01048-2>

**INTRODUCTION**

The endoplasmic reticulum (ER) forms a continuous membrane system, consisting of the nuclear envelope, flattened sheets, and interconnected tubules that spread over the cytosol [1–3]. This distribution of ER tubules requires continuous remodeling as new ER tubules grow out of existing ones, old tubules retract, sheets move, and new junctions are formed by tethering and/or fusion between ER membranes [4, 5].

ER tubules form membrane contact sites (MCSs) with the same or other organelles [6, 7]. ER tubules can be tethered and fused between two identical ER membranes [8–11]. The homotypic ER tethering and fusion is mediated by Atlastins (ATLs), a class of highly conserved, dynamin-like GTPase [8, 12], and stabilized by Lunapark (Lnp) [13]. The tethering between two identical ER tubules generates a transient structure, named three-way ER junctions, intra-ER contacts or ER branches [6, 8, 9, 12, 14]. The tethering between ER tubules is important since the periphery ER network is suggested to be dominantly maintained by the transient tethering rather than fusion [9, 10]. Besides, ER tubules can be tethered to other organelles, so that the two organelles will remain associated as they traffick along microtubules [6, 7, 15]. For instance, ER-mitochondria MCSs are microdomains where the ER membrane and the outer mitochondrial membrane (OMM) are closely apposed and tethered with gap distance of 10–30 nm, but do not fuse [16, 17].

The formation of ER contacts requires tethers, a complex of proteins that specifically localize to the contacts and increase the

affinity of one organelle for another [6, 18]. To date, a couple of tethers of ER-mitochondria MCSs have been identified, including the ER-mitochondria encounter complex (ERMES) in yeast [19], mitofusin 2 (MFN2) [20], VDAC-GRP75-IP3R [21], Fis1-Bap31 [22], VAPB-PTPIP51 [23], and VPS13A [24] in mammals. Compared with ER-mitochondria MCSs, the formation of three-way ER junctions is less well understood.

Previous studies have shown that an ESCRT protein CHMP7 couples with LEM2, a transmembrane ESCRT adaptor on the nuclear envelope, coordinates an ESCRT-III dependent nuclear envelope reformation at mitotic exit [25–28]. In this study, we showed that CHMP7 mediated three-way ER junctions and ER-mitochondria interactions at non-mitotic stages. We demonstrated that CHMP7 underwent dynamic assemblies at these ER contacts through C-terminal (CT) CHMP-like domain-dependent oligomerization. CHMP7 mediated the formation of three-way ER junctions independently of ATLs, and also regulated ER-mitochondrial interactions and its depletion affected mitochondrial division and function independently of ESCRT complex.

**RESULTS****CHMP7 localizes to the ER, MAMs and the OMM**

To explore the functions of CHMP7 at non-mitotic stages, we initiated with examining its expression during the cell cycle (Fig. S1A). CHMP7 was constitutively expressed during the cell

<sup>1</sup>Department of Biochemistry and Molecular Biology, School of Basic Medicine, Tongji Medical College, Huazhong University of Science and Technology, Wuhan, China. <sup>2</sup>Cell Architecture Research Center, Huazhong University of Science and Technology, Wuhan, Hubei 430030, China. <sup>3</sup>Department of Anesthesiology, Tongji Hospital, Tongji Medical College, Huazhong University of Science and Technology, Wuhan, Hubei 430030, China. <sup>4</sup>Shenzhen Bay Laboratory, Shenzhen 518132, China. <sup>5</sup>These authors contributed equally: Qingzhu Chu, Jingru Wang. ✉email: Juanxiong1207@163.com; Weike\_ji1985@163.com; denglin@szbl.ac.cn Edited by L. Scorrano

Received: 17 February 2022 Revised: 1 July 2022 Accepted: 20 July 2022

Published online: 12 August 2022

cycle (Fig. S1B). Interestingly, CHMP7 was highly expressed in the brain and testes of mice (Fig. S1C).

We next investigated the localization of exogenous CHMP7-Falg in interphase COS7 cells using immunofluorescence (IF) as cells in interphase were flat and suitable for imaging. CHMP7-Flag associated with the ER and formed punctate structures (Fig. 1A, C). Surprisingly, a significant portion of the CHMP7 puncta (~40%) localized to ER-mitochondrial junctions (Fig. 1B, D).

To avoid the potential artifacts of overexpression, we tagged endogenous CHMP7 with a N-terminal Halo tag by CRISPR/Cas9 knock-in technique (Halo-CHMP7 KI) in human retinal pigment epithelial RPE1 cells (Fig. S2). We tagged Halo tag to the N-terminus of CHMP7 as the N-terminal tagging colocalized with CHMP7-Flag to a higher extent than the C terminal tagging (Fig. S3). Endogenous Halo-CHMP7 formed 'puncta' of varying intensity (Fig. 1E), likely representing CHMP7 oligomers. Consistently, >90% of endogenous Halo-CHMP7 oligomers localized to the ER (Fig. 1F), with ~20% of puncta at ER-mitochondria junctions (Fig. 1G, J). Strikingly, ~60% of all the puncta (Fig. 1H), and ~70% of those ER-associated puncta (Fig. 1I), were present at 3-way ER junctions, or ER branches.

Next, for time-lapse imaging we generated a stable COS7 line expressing CHMP7 with N-terminal monomeric (A206K) GFP tags under the control of a tetracycline-inducible promoter (Tet-on GFP-CHMP7 line). Previous studies suggested that forced high expression of ESCRT-III proteins fused with fluorescent proteins might exhibit dominant-negative effects [29]. To minimize the effect, we titrated the induction conditions. A low concentration (0.5  $\mu$ M) of doxycycline (DOX) with a short incubation time (6 h) was applied because the level of GFP-CHMP7 is comparable to that of endogenous CHMP7 along with a satisfactory imaging quality (Fig. 1K). We used this condition for the imaging of GFP-CHMP7 dynamics thereafter unless otherwise stated.

Furthermore, we tracked CHMP7 puncta relative to ER-mitochondrial MCSs over time. GFP-CHMP7 puncta were specifically localized to ER-mitochondria junctions, and these CHMP7-marked junctions were stable as the ER and mitochondria were moving over time (Fig. 1L; Supplementary Video 1).

We next explored the cellular distribution of endogenous, unlabeled CHMP7 by cell fractionation (Fig. S4). The mouse brain was prepared for our samples as CHMP7 was highly expressed in the brain (Fig. S1C). CHMP7 was mainly present in the ER and the cytosol. Importantly, consistent with our imaging results, a small but substantial portion of CHMP7 was enriched in the mitochondrial associated membranes (MAMs) [30] (Fig. 1M). Interestingly, a portion of CHMP7 was also in pure mitochondrial fractions (Fig. 1M). These results suggested that CHMP7 localizes to the ER, MAMs and the OMM.

### CHMP7 undergoes dynamic assemblies at three-way ER junctions and ER-mitochondria MCSs

We examined CHMP7 dynamics by super-resolution microscopy. Consistently, a great portion of ER-associated GFP-CHMP7 puncta (~60%) were stably present at three-way ER junctions over time (Fig. 2A, C; Supplementary Video 2).

Strikingly, GFP-CHMP7 puncta were able to merge (arrows in Fig. 2D, E), resembling the 'maturation' process of large GTPase dynamin-like protein Drp1 on the OMM [31], likely through oligomerization. Indeed, CHMP7 oligomerization was reported in CHMP7-coordinated nuclear envelope reformation during mitotic exit [27]. Importantly, multiple ER tubules gradually assembled, and then appeared to form sheet-like structures or ER tubule bundles, as GFP-CHMP7 puncta merged (Fig. 2D, E; Supplementary Videos 3 and 4).

Importantly, the assembly of GFP-CHMP7 puncta could also occur at ER-mitochondrial junctions. GFP-CHMP7 gradually

assembled at ER-mitochondria junctions, and the latter were gradually increased as CHMP7 puncta merged (Fig. 2F, G; Supplementary Video 5).

Next, we explored GFP-CHMP7 dynamics by fluorescence recovery after photobleaching (FRAP). Most GFP-CHMP7 puncta fluorescence recovered to ~80% of the original level in 5 min (Fig. 2H, I), suggesting a possible translocation of the protein from the ER or the cytosol. Two CHMP7 mutants (V339D R270E; I312E R270E), deficient in binding to LEM2, were still able to recover but to a less extent (Fig. 2H, I). Altogether, our results suggested that CHMP7 undergoes dynamic assemblies at ER contacts.

### The $\alpha$ helices-1 & 2 of CHMP7-CT are responsible for CHMP7 assembly at contacts

To understand how CHMP7 assembled at ER contacts, we dissected CHMP7. CHMP7 contains an extended NT consisting of tandem winged-helix domains responsible for its membrane binding, making it unique among ESCRT-III subunits [28]. The CHMP7-CT contains six  $\alpha$  helices belonging to CHMP-like domain required for ESCRT-III interactions [29] (Fig. S5A). CHMP7-NT was evenly distributed along the ER network (Fig. 3A), in accord with a previous study [28]. Intriguingly, CHMP7-NT could also homogeneously target the OMM (Fig. 3A), consistent with cell fractionation results (Fig. 1M). In contrast, CHMP7-CT was mainly cytosolic (Fig. 3B). The cellular localizations of CHMP7-NT and CHMP7-CT were further confirmed by cell fractionation (Fig. S5B–D).

Given that the homogenous distribution of CHMP7-NT on membranes, we hypothesized that CHMP7-CT might be critical for CHMP7 oligomerization at contacts. Indeed, GFP trap assays showed that Halo-CHMP7 interacted with GFP-CHMP7 exclusively via CHMP7-CT (Fig. 3C, D). The  $\alpha$  helices 1-2, but not the  $\alpha$  helices 3-6, of the CHMP7-CT, were responsible for CHMP7 oligomerization (Fig. 3E, F). Notably, deletion of  $\alpha$  helix-2 almost completely abolished CHMP7 oligomerization, while deletion of  $\alpha$  helix-1 also reduced the extent of CHMP7 oligomerization but to a less extent than that of  $\alpha$  helix-2 (Fig. 3G, S5E). Notably, neither  $\alpha$  helix-1 nor  $\alpha$  helix-2 alone was sufficient to interact with full-length CHMP7 (Fig. S5F). Furthermore, purified Glutathione S-transferase (GST) tagged CHMP7 directly bound to His-CHMP7 or His-CHMP7-CT (Fig. 3H), and GST-CHMP7-CT bound to His-CHMP7-CT (Fig. 3I). We further explored the localizations of the oligomerization-defective CHMP7 mutants, CHMP7- $\Delta\alpha$ 1 and CHMP7- $\Delta\alpha$ 2. Notably, both mutants were mainly cytosolic with a portion being homogenous over the membranes (Fig. 3J, K).

### The hydrophobic residues in $\alpha$ helix-2 are required for CHMP7 assembly at contacts

Next, we sought to identify the residues in  $\alpha$  helix-2 critical for CHMP7 oligomerization. Conserved residues were identified via alignments of the helix-2 from different species (Fig. 4A and S6A). We created two types of CHMP7 mutants: an electrostatic mutant (mut-1), and two amphipathic mutants (mut-2 & 3). The interactions between wild type (WT) CHMP7 and CHMP7-mut2 & 3 was greatly reduced (Fig. 4B), while oligomerization of CHMP7-mut1 was not substantially affected (Fig. 4B). Furthermore, the mut-1 was still able to form puncta at ER contacts (Fig. 4C, D). However, mut-2/3 was homogeneously distributed over the ER and the OMM (Fig. 4C, E, & F). Together, these results indicated that the hydrophobic residues are essential for the oligomerization and localizations of CHMP7 at contacts.

We next confirmed the localization of CHMP7 mutants by cell fractionations. Consistent with endogenous, untagged CHMP7, GFP-CHMP7 was primarily present in the ER and the cytosol, and a significant portion was present in both pure mitochondria and MAM fractions. However, CHMP7-mut2 was almost undetectable in the MAM fraction (Fig. 4G & S6B), confirming that the

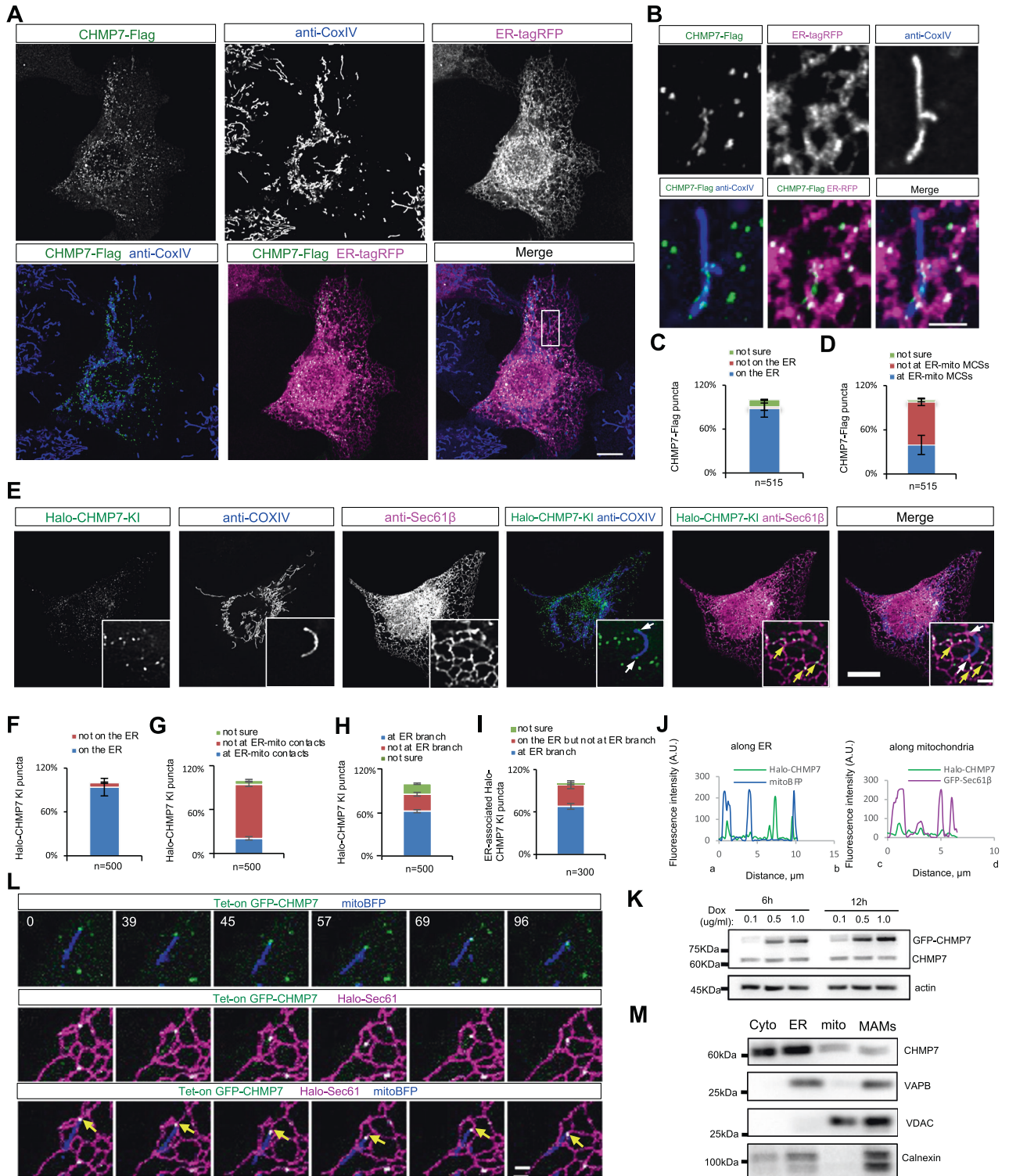


**Fig. 1** The localization of CHMP7 relative to the ER, and ER-mitochondrial MCSs. **A, B** Confocal images of fixed COS7 cells expressing CHMP7-Flag (anti-Flag, green), ER-tagRFP (magenta), and immunostained with anti-CoxIV (mitochondrial marker, blue) with a boxed region shown in **(B)**. **C, D** Quantification of CHMP7-Flag puncta relative to the ER (**C**) or to the ER-mitochondrial MCSs (**D**). Mean  $\pm$  SD. **E** Confocal images of a fixed Halo-CHMP7-KI (green) RPE1 cell immunostained using anti-Sec61 $\beta$  antibodies (the ER marker, magenta) and anti-COXIV (mitochondrial matrix marker, blue) with white arrows denoting Halo-CHMP7 puncta at potential ER-mitochondrial MCSs and yellow arrows indicating CHMP7 puncta at ER branches. **F–I** Quantification of endogenous Halo-CHMP7 puncta relative to the ER (**F**), the ER-mitochondrial MCSs (**G**), ER branches (**H**), or to the ER but not ER branches (**I**). Mean  $\pm$  SD. **J** Line-scan analysis along the ER tubule (Left) or mitochondria (Right) showing the presence of Halo-CHMP7 puncta at ER-mitochondrial MCSs. **K** Western blots demonstrate the tet-on inducible expression of GFP-CHMP7 relative to endogenous CHMP7 in COS7 cells using anti-CHMP7 antibodies. **L** Time-lapse images of a COS7 cell expressing Halo-Sec61 (magenta), mitoBFP (blue), and Tet-on GFP-CHMP7 (0.5 ug/ml; 6 h; green) with yellow arrows denoting that a GFP-CHMP7 puncta stably associates with ER-mitochondrial MCSs over time. **M** Western blots show the distribution of endogenous CHMP7 in membrane fractions isolated from mouse brain lysates. Scale bar, 10  $\mu$ m in **(A, E)** and 2  $\mu$ m in insets in **(E)**, and **(B, L)**. Time in sec.



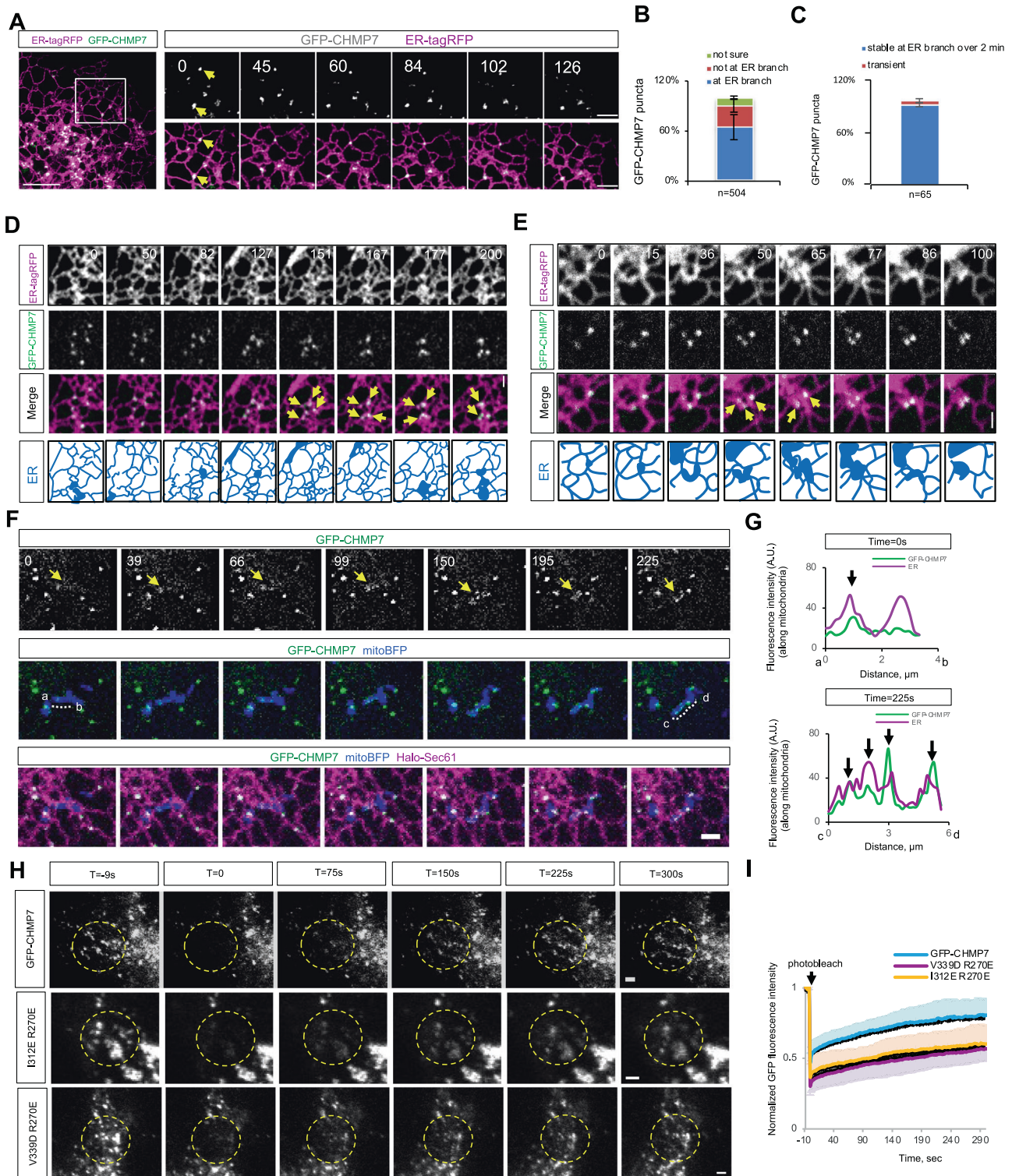


**Fig. 2** Dynamic assembly of CHMP7 at the three-way ER and ER-mitochondrial MCSs. **A** Left: High-resolution images show a COS7 cell expressing Tet-on GFP-CHMP7 (0.5  $\mu\text{g/ml}$ ; 6 h; green) and ER-tagRFP (magenta); right: time-lapse images from a boxed region in the whole-cell image with yellow arrows indicating GFP-CHMP7 puncta stably associating with ER branches over time. **B** Quantification of Tet-on GFP-CHMP7 puncta relative to ER branches. Mean  $\pm$  SD. **C** Percentage of Tet-on GFP-CHMP7 puncta stably at ER branches over 2 min. Mean  $\pm$  SD. **D**, **E** Time-lapse images of COS7 cells expressing Tet-on GFP-CHMP7 (0.5  $\mu\text{g/ml}$ ; 6 h; green) and ER-tagRFP (magenta) with yellow arrows denoting that GFP-CHMP7 puncta dynamically assemble along with the formation of three-way ER junctions. **F** Time-lapse images of COS7 cells expressing Tet-on GFP-CHMP7 (0.5  $\mu\text{g/ml}$ ; 6 h; green), mitoBFP (blue), and ER-tagRFP (magenta) with yellow arrows denoting that GFP-CHMP7 puncta dynamically assemble as ER-mitochondria MCSs increase. **G** Line-scan analysis of GFP-CHMP7 puncta at ER-mitochondrial MCSs at  $t = 0$  s (top) and  $t = 255$  s (bottom) with black arrows denoting GFP-CHMP7 puncta at contacts. **H** FRAP assays of COS7 cells expressing either Tet-on GFP-CHMP7 (0.5  $\mu\text{g/ml}$ ; 6 h; top), Tet-on GFP-CHMP7 V339D R270E (0.5  $\mu\text{g/ml}$ ; 6 h; middle), or Tet-on GFP-CHMP7 I312E R270E (0.5  $\mu\text{g/ml}$ ; 6 h; bottom). Fluorescence of ROIs is photobleached at time = 0. **I** Normalized GFP fluorescence of Tet-on GFP-CHMP7 and mutants ( $n = 8$  ROIs) before and after photobleach. Mean  $\pm$  SD. Scale bar, 2  $\mu\text{m}$  in **(A, D–F, & G, H)**. Time in sec.



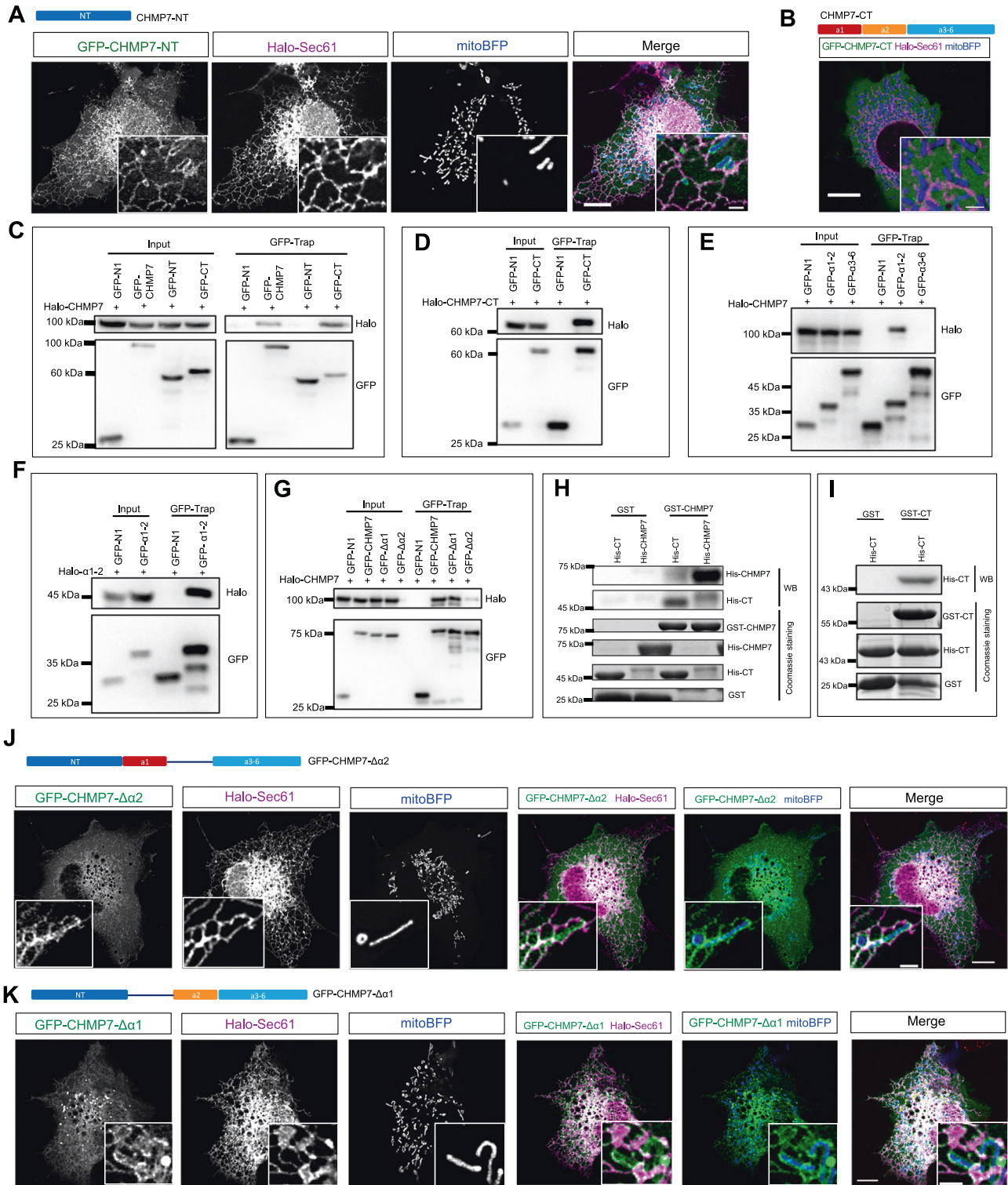


**Fig. 3** The assembly of CHMP7 at ER contacts requires helices 1&2 of CT domain. **A** Confocal images show a COS7 cell expressing GFP-CHMP7-NT (green), Halo-Sec61 (magenta), and mitoBFP (blue) with insets. **B** Confocal images show a COS7 cell expressing GFP-CHMP7-CT (green), Halo-Sec61 (magenta), and mitoBFP (blue) with an inset. **C** GFP-Trap assays show that GFP-CHMP7-CT, but not GFP-CHMP7-NT, interacts with the full-length GFP-CHMP7. **D** GFP-Trap assays show that GFP-CHMP7-CT interacts with itself. **E** GFP-Trap assays show that the  $\alpha$ 1-2 helices of CT domain, but not the  $\alpha$ 3-6 helices, are able to interact with the full-length GFP-CHMP7. **F** GFP-Trap assays show that the  $\alpha$ 1-2 helices interact with itself. **G** GFP-Trap assays show that the  $\alpha$  helix-2 is indispensable for self-interactions. **H** GST pull-down assays of purified His-CHMP7, or His-CHMP7-CT interacting with GST-CHMP7 in vitro using GST tag as a negative control. **I** GST pulldown assays of purified His-CHMP7-CT interacting with GST-CHMP7-CT in vitro using GST tag as a negative control. **J, K** Confocal images show BODIPY (red)-loaded COS7 cells expressing Tet-on GFP-CHMP7- $\Delta\alpha$ 2 (green, **J**) or Tet-on GFP-CHMP7- $\Delta\alpha$ 1 (green, **K**), Halo-Sec61 (magenta), and mitoBFP (blue) with insets. Scale bar, 10  $\mu$ m in whole cell image and 2  $\mu$ m in insets in (**A, B, J, & K**).

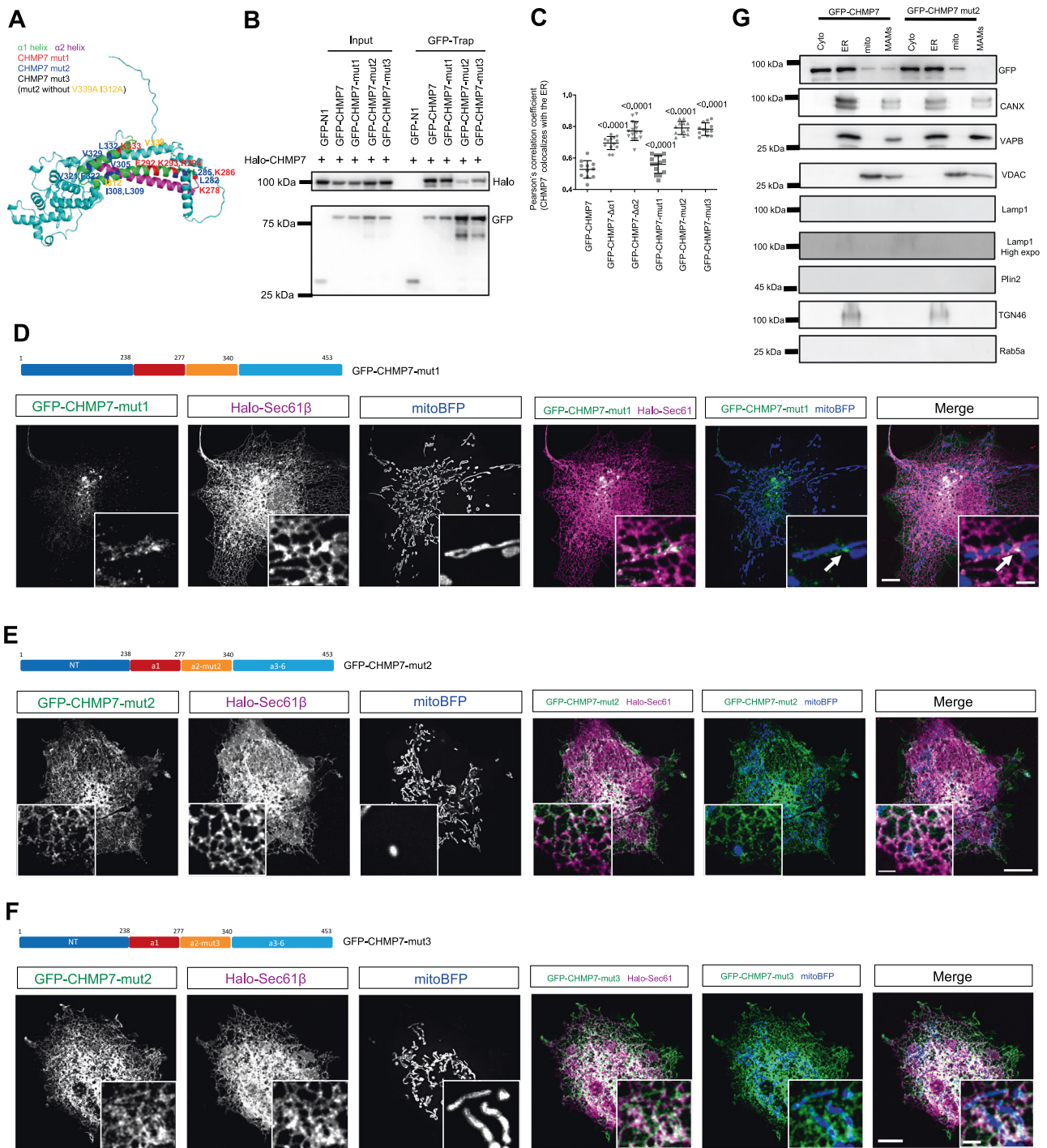
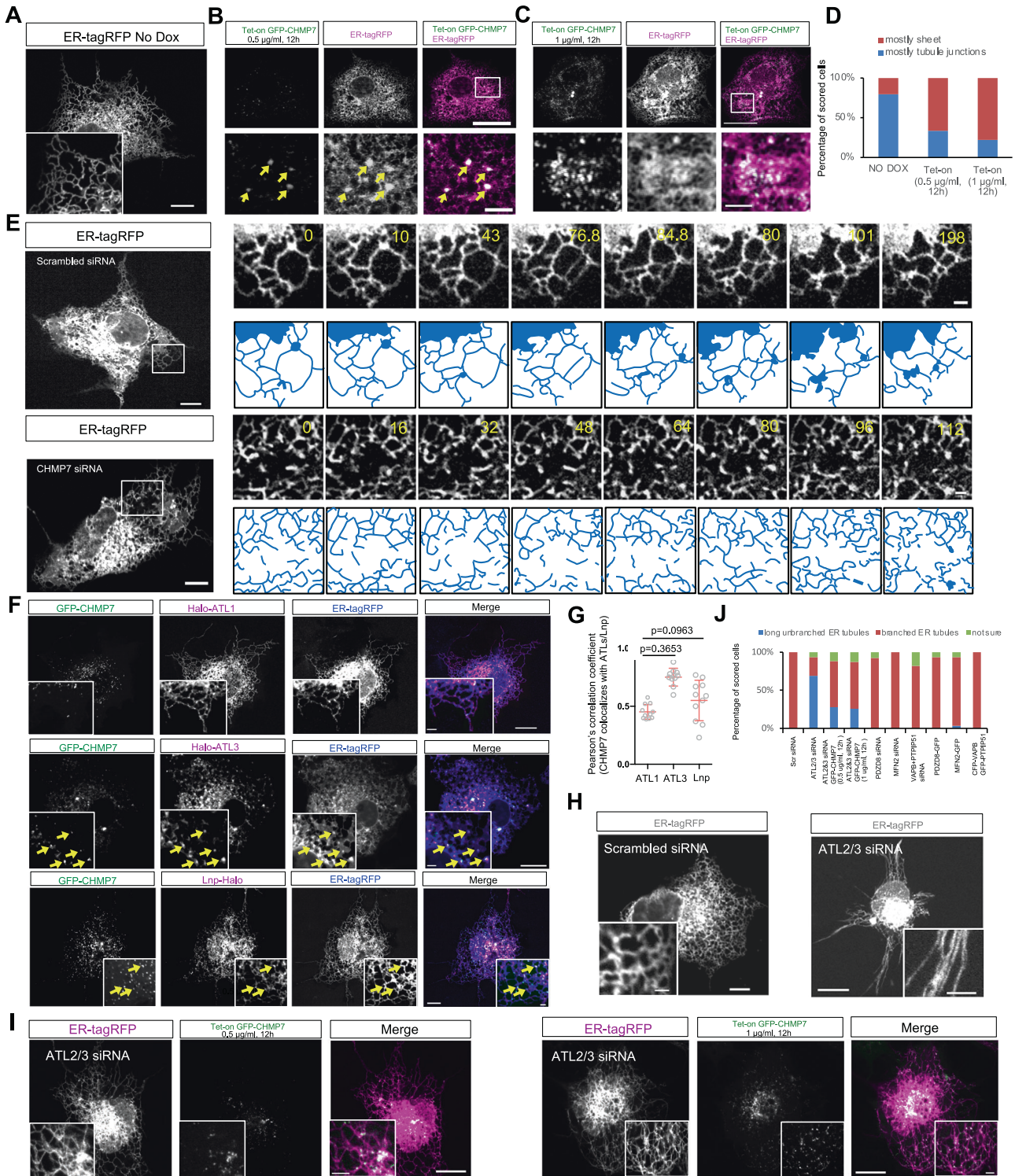


**Fig. 4** The hydrophobic residues of the two  $\alpha$  helices are responsible for CHMP7 assembly at contacts. **A** AlphaFold-predicted protein structure [46] of human CHMP7 with conserved charged residues (mut1; K278E; K286E; E292K; K293E; R294E; K333E) in red, and two hydrophobic mutants (mut2: L282A; L285A; V305A; I308A; L309A; I312A; V321A; F322A; V329A; L332A; V339A; mut3: L282A; L285A; V305A; I308A; L309A; V321A; F322A; V329A; L332A) residues in blue, of the  $\alpha$ 2 helix. **B** GFP-Trap assays show that the hydrophobic residues mutated in mut2 and mut3 were indispensable for CHMP7 oligomerization while the oligomerization of electrostatic mut1 was only moderately reduced. **C** Pearson's correlation coefficient between GFP-CHMP7 and its mutants and the ER from more than 3 independent experiments. Ordinary one-way ANOVA with Tukey's multiple comparisons test. Mean  $\pm$  SD. **D–F** Confocal images show COS7 cells expressing Tet-on GFP-CHMP7-mut1 (green, **D**), Tet-on GFP-CHMP7-mut2 (green, **E**), or Tet-on GFP-CHMP7-mut3 (green, **F**), Halo-Sec61 (magenta), and mitoBFP (blue) with insets. White arrows indicate a GFP-CHMP7 puncta at ER-mitochondrial junction. **G** Western blots show the distribution of GFP-CHMP7 and GFP-CHMP7-mut2 in membrane fractions isolated from HEK293 cells transfected with CHMP7 constructs. Scale bar, 10  $\mu$ m in whole cell image and 2  $\mu$ m in insets in (**D–F**).





hydrophobic residues are essential for CHMP7 localizations at MAMs.

### The two $\alpha$ helices are required for tethering different organelles in vivo

The assembly of CHMP7 at ER contacts suggested a potential role of CHMP7 in the formation of these contacts. Therefore, we investigated CHMP7's ability to tether the ER to other organelles in vivo using G/RFP nanobodies (G/RFPnb)-based recruitment strategy (Fig. S7). Strikingly, the ER, marked by Halo-CHMP7 or

Halo-CHMP7-CT, was completely tethered to the OMM, lysosome, or LD membranes when GFP-CHMP7-CT was artificially targeted to these membranes via G/RFPnb (Fig. S7A–H). However, CHMP7- $\Delta\alpha 2$  almost completely lost the tethering activity (Fig. S7J, K), while CHMP7- $\Delta\alpha 1$  reduced the tethering of the ER to mitochondria (Fig. S7I, K). In addition, LEM2 depletion by small interfering RNAs (siRNA) failed to inhibit the tethering of Halo-CHMP7-marked ER to the OMM (Fig. S8). These results suggested that CHMP7 oligomerization is able to tether organelles to the ER independently of LEM2.

**Fig. 5 CHMP7 regulates the formation of 3-way ER junctions.** **A** Whole-cell image of a Tet-on GFP-CHMP7 COS7 cell expressing ER-tagRFP in absence of Dox with an inset showing peripheral ER. **B, C** Representative confocal images of Tet-on GFP-CHMP7 COS7 cells expressing GFP-CHMP7 in either mild (0.5  $\mu\text{g}/\text{ml}$ , 12 h, **B**) or high (1  $\mu\text{g}/\text{ml}$ , 12 h, **C**) induction conditions as well as ER-tagRFP with insets showing peripheral ER. Yellow arrows indicate GFP-CHMP7 puncta relative to the ER. **D** Quantification of scored cells in the morphology of periphery ER in response to no DOX ( $n = 73$  cells), mild ( $n = 63$  cells), and high ( $n = 73$  cells) induction of GFP-CHMP7. **E** Representative confocal images of COS7 cells expressing ER-tagRFP upon scrambled (top) or CHMP7 (bottom) siRNA treatments. Left: whole-cell images; right: time-lapse images of boxed regions showing the dynamics of ER tubules at periphery. **F** Confocal images of COS7 cell expressing Tet-on GFP-CHMP7 (0.5  $\mu\text{g}/\text{ml}$ ; 12 h; green), and either Halo-ATL1 (magenta; top panel), Halo-ATL3 (magenta; middle panel) or Lnp-Halo (magenta; bottom panel) as well as ER-tagRFP (blue) with insets showing GFP-CHMP7 puncta relative to ATLs/Lnp at periphery ER. Yellow arrows indicate the colocalization between GFP-CHMP7 and ATL3-Halo. **G** Pearson's correlation coefficient between GFP-CHMP7 and ATLs/Lnp from more than 3 independent experiments. Ordinary one-way ANOVA with Tukey's multiple comparisons test. Mean  $\pm$  SD. **H** Confocal images of COS7 cells expressing ER-tagRFP upon scrambled (left) or ATL 2/3 siRNAs (right) treatments with insets showing periphery ER. **I** Confocal images of Tet-on GFP-CHMP7 COS7 cells expressing GFP-CHMP7 in a mild level (0.5  $\mu\text{g}/\text{ml}$ , 12 h; green; left) or in a high level (1  $\mu\text{g}/\text{ml}$ , 12 h; green; right), and ER-tagRFP (magenta) upon ATL2/3 siRNAs treatments with insets showing periphery ER. **J** Quantification of scored cells in the morphology of periphery ER in response to scrambled ( $n = 17$  cells), ATL2/3 siRNAs ( $n = 48$  cells), ATL2/3 siRNA followed by Tet-on GFP-CHMP7 (mild,  $n = 43$  cells; high,  $n = 54$  cells), PDZD8 siRNA ( $n = 47$  cells), MFN2 siRNA ( $n = 35$  cells), VAPB + PTPIP51 siRNA ( $n = 38$  cells), PDZD8-GFP ( $n = 29$  cells), MFN2-GFP ( $n = 20$  cells), or CFP-VAPB + GFP-PTPIP51 ( $n = 15$  cells). Scale bar, 10  $\mu\text{m}$  in whole cell image and 2  $\mu\text{m}$  in insets. Time in sec.

### CHMP7 mediates the formation of three-way ER junctions in parallel with ATLs

We next investigated whether CHMP7 mediated the formation of three-way ER junctions. The periphery ER formed a delicate tubule-sheet network, with tubules forming extensive three-way junctions in control cells (Fig. 5A). A mild level of GFP-CHMP7 (0.5  $\mu\text{g}/\text{mL}$ , 12 h) caused sheet-like ER structures concomitant with GFP-CHMP7 enrichments (Fig. 5B). The amount of the sheet-like ER structures was proportional to GFP-CHMP7 level (Fig. 5C, D).

To test whether CHMP7 is a structural tether of three-way ER junctions, we examined the dynamics of ER tubules at cell periphery in control or CHMP7-depleted COS7 cells. In control, ER tubules kept growing and retracting; new junctions were formed by contacting and/or fusing between ER membranes, followed by forming ER sheets (Fig. 5E, top panel). In contrast, ER tubules in CHMP7-depleted cells appeared to be less interconnected in some areas (Fig. 5E, bottom panel). Although the ER tubules in these cells were still actively motile, they failed to form long-lasting three-way ER junctions (Supplementary video 6).

Since ATLs and Lnp mediated three-way ER junctions in metazoans [8, 12, 13], we attempted to explore the relationship between CHMP7 and ATLs/Lnp. Halo-ATL1 was evenly distributed over the ER (Fig. 5F; top panel), whereas a portion of Halo-ATL3 colocalized with GFP-CHMP7 puncta at three-way ER junctions (Fig. 5F, G; middle panel). Although GFP-CHMP7 partially co-localized with Lnp-Halo (Fig. 5F, G), Lnp depletion did not abolish the presence of GFP-CHMP7 at ER contacts (Fig. S9A–C), indicating that the presence of GFP-CHMP7 at ER contacts is independent of Lnp.

Importantly, upon ATL2/3 depletion, the periphery ER network was extensively remodeled with long unbranched ER tubules in ~69% of scored cells (Fig. 5H, J), suggesting a lack of ER tubule tethering and/or fusion, agreeing with previous studies [8, 32]. Then, we examined whether CHMP7 could rescue the ER defects resulted from ATL2/3 depletion in COS7 cells. Although the periphery ER remained abnormal even upon GFP-CHMP7 expression in ATL2/3-depleted cells (Fig. 5I), expression of GFP-CHMP7 in a mild (Fig. 5I) or a higher level (Fig. 5I) indeed resulted in more branched ER tubules or ER tubule bundles with specific enrichments of GFP-CHMP7 at these junctions in ~60% of scored cells (Fig. 5I, J). In addition, we observed that modulation of other ER contact proteins, including PDZD8 [33], MFN2 [20], or VAPB and PTPIP51 [23] did not substantially affect periphery ER morphology (Fig. 5J & S9D), suggesting a specific role of CHMP7 in regulating ER morphology. Collectively, these results suggested that CHMP7 promotes the formation of three-way ER junctions in parallel with ATLs.

### CHMP7 regulates ER-mitochondria interactions

The presence of CHMP7 puncta at ER-mitochondria junctions led us to hypothesize that CHMP7 might regulate such MCSs. Strikingly,

ER-mitochondria associations were substantially increased upon a high level of GFP-CHMP7 (1  $\mu\text{g}/\text{mL}$ , 12 h), with mitochondria being surrounded by the ER (Fig. 6A, B). A great portion of GFP-CHMP7 puncta (~60%) specifically enriched at contacts (Fig. 6C, D), which was also the case for a mild (Fig. 6E) or a low expression of GFP-CHMP7 (Fig. 6F). In addition, mitochondria appeared to be fragmented in cells highly overexpressing GFP-CHMP7 (Fig. 6A, B).

Importantly, we directly examined ER-mitochondria interactions by transmission electron microscopy (TEM). The ER extensively contacted with mitochondria, upon the induced expression of GFP-CHMP7 (1  $\mu\text{g}/\text{mL}$ , 12 h) in Tet-on GFP-CHMP7 COS7 cells (Fig. 6G, H).

Next, we used in situ proximity ligation assays (PLA) to examine the role of CHMP7 on ER-mitochondria interactions in HEK293 cells. Importantly, depletion of CHMP7 substantially reduced the number of PLA puncta (Fig. 6I, J), similar as that of VAPB-PTPIP51 depletion (Fig. 6I, J), which was a well-studied tether complex at ER-mitochondrial MCSs [23].

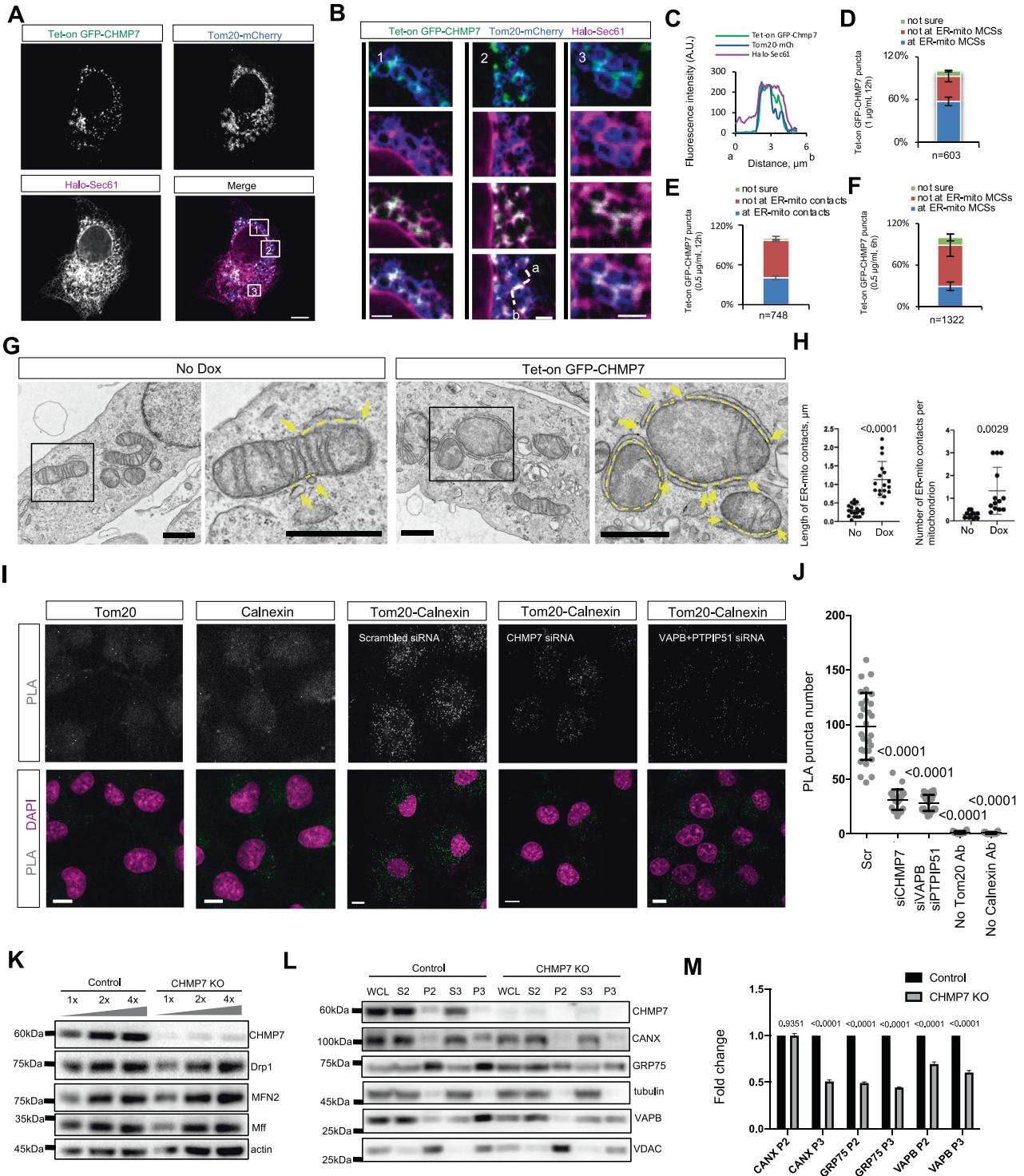
We further confirmed the effects of CHMP7 depletion on ER-mitochondria interactions by cell fractionation. To this end, we generated a pool of CHMP7 knockout HEK293 cells (CHMP7 KO) using CRISPR/Cas9 (Fig. 6K). ER-mitochondria interactions were significantly reduced in CHMP7 KO cells, as revealed by reduced amounts of MAM proteins, which were normalized to the level of whole cell lysates, in crude mitochondrial membrane fractions P2 and P3 (Fig. 6L, M). Thus, these results supported that CHMP7 is required for the proper ER-mitochondria interactions. Notably, our results did not exclude the possibility that CHMP7 indirectly regulate the ER-mitochondrial interactions through modulating the morphology of the ER or mitochondria, since inter-organelle contacts, especially ER-mitochondria contact sites, are profoundly affected by changes in the basal morphology of one or another organelle.

### CHMP7 affects mitochondrial division

ER-mitochondria MCSs play an essential role in mitochondrial division [17]. Our results showed that overexpression of CHMP7 appeared to cause mitochondrial fragmentation (Fig. 6A, B), suggesting a role of CHMP7 in mitochondrial dynamics. Indeed, CHMP7 depletion resulted in a significant increase in mitochondrial length in both COS7 and U2OS cells (Fig. S10A–F). In addition, the morphology and size of other organelles, including LD, the Golgi, peroxisome, and lysosome, were not substantially affected upon either CHMP7 depletion or CHMP7 overexpression (Fig. S11).

Consistently, CRISPR/Cas9-mediated CHMP7 KO resulted in a significant increase in mitochondrial length in HEK293 cells. GFP-CHMP7 significantly rescued the mitochondrial length. However, CHMP7- $\Delta\alpha 2$  failed to restore the phenotype, while CHMP7- $\Delta\alpha 1$  only had a moderate rescuing effect. Importantly, GFP-CHMP7-mut2 failed to restore the phenotype (Fig. 7A, B). Furthermore, the





CHMP7 mutants deficient of LEM2 binding, including I312W/V339D, I312E/R270E, and R270E/V339D [27], and the CDK1-phosphorylation mimic mutant, S441D [25] (Fig. 7C), could significantly rescue this phenotype. Moreover, GFP trap assays indicated that two ER membrane-binding dead mutants, GFP-CHMP7-L127A and GFP-CHMP7 ( $\Delta$ 118-128) [28], were able to interact with Halo-CHMP7 (Fig. S10G), suggesting that CHMP7 oligomerization is separable from its ER membrane binding. Altogether, CHMP7 oligomerization is required for its regulation of mitochondrial dynamics.

Video analyses showed that a small portion of CHMP7 puncta were at ER-mitochondria MCSs where mitochondrial divisions were about to occur (Fig. 7D; Supplementary Video 7), suggesting a direct role of CHMP7 in mitochondrial division. In addition, CHMP7 depletion also increased mitochondrial length in intestines of *Caenorhabditis elegans* (Fig. 7E–G), meanwhile ER morphology seems abnormal in CHMP7 RNAi worms (Fig. 7F, G). These results suggested a conserved role of CHMP7 in these processes.

Next, we sought to understand how CHMP7 affected mitochondrial division. CHMP7 depletion did not affect the levels of

**Fig. 6 CHMP7 regulates ER-mitochondrial interactions.** **A** Whole-cell image of a COS7 cell expressing Tet-on GFP-CHMP7 (1 ug/ml; 12 h; green), Halo-Sec61 (magenta), and Tom20-mCh (blue). **B, C** As in **(A)**, ROIs from three boxed regions in **(A)** are shown with line-scan analysis demonstrating the enrichment of GFP-CHMP7 at ER-mitochondrial MCSs **(C)**. **D–F** Quantification of Tet-on GFP-CHMP7 puncta upon either high induction (1 ug/ml; 12 h; **D**), mild induction (0.5 ug/ml; 12 h; **E**), or low induction (0.5 ug/ml; 6 h; **F**) relative to ER-mitochondrial MCSs. Mean  $\pm$  SD. **G** Representative TEM micrographs showing examples of ER-mitochondrial MCSs in control or Tet-on GFP-CHMP7 (1 ug/ml; 12 h; green) cells with an inset on right. Examples of ER-mitochondrial MCSs are indicated by yellow arrows, and yellow dash lines indicate the extension of ER-mitochondrial MCSs. These MCSs under TEM were defined as regions within 30 nm gaps between the ER and the OMM. **H** Quantification of length of ER-mitochondria MCSs (left panel) and number of ER-mitochondria MCSs per mitochondrion (right panel). Control cells ( $n = 19$  MCSs) and Tet-on GFP-CHMP7 cells ( $n = 17$  MCSs) are analyzed. Two-tailed unpaired Student's  $t$  test. Mean  $\pm$  SD. **I** In situ proximity ligation assays of HEK293 cells treated with scrambled, CHMP7 siRNA, or VAPB + PTPIP51 siRNAs using anti-Tom20 antibodies and anti-Calnexin. Nucleus were stained by DAPI (magenta). **J** Quantification of PLA puncta in two negative controls either without anti-Tom20 antibodies ( $n = 20$  cells) or without anti-Calnexin ( $n = 20$  cells), and in cells upon scrambled ( $n = 28$  cells), CHMP7 siRNA ( $n = 24$  cells), or VAPB + PTPIP51 siRNAs ( $n = 27$  cells) from 3 independent experiments. Ordinary one-way ANOVA with Tukey's multiple comparisons test. Mean  $\pm$  SD. **K** Western blots show the expression level of CHMP7, Drp1, MFN2, Mff and actin in control or Crispr-cas9-mediated CHMP7 KO HEK293 cells. Three amounts (1x, 2x, and 4x) of samples were loaded. **L** Western blots show the distribution of CHMP7 in membrane fractions isolated from either control or CHMP7 KO HEK293 cell lysates. **M** Quantification of the levels of MAM markers (Calnexin, Grp75 and VAPB) in the P2 (heavy membrane fractions) or P3 (enriched heavy membrane fractions) in control or CHMP7 KO cells. The ratio was normalized to the amounts of Calnexin, Grp75 and VAPB in WCL from 3 independent experiments. Ordinary one-way ANOVA with Tukey's multiple comparisons test. Mean  $\pm$  SD. Scale bar, 10  $\mu$ m in **(A & I)** and 1  $\mu$ m **(G)**.

mitochondrial dynamics proteins including Drp1, MFN2 and Mff (Fig. 6K), and CHMP7 did not interact with these proteins (Fig. S12A). In addition, CHMP7 did not regulate mitochondrial division through ESCRT complex (Fig. S12B–O).

Since ER-mitochondrial MCSs are essential for the assembly of productive Drp1 oligomers [31, 34], we tested the density of Drp1 and its key adaptor Mff [35] on the OMM upon CHMP7-depletion. CHMP7 depletion significantly reduced both mitochondria-associated Drp1 puncta (Fig. S13A, B) and Mff puncta (Fig. S13C, D). Notably, mechanisms underlying the CHMP7-mediated regulation of mitochondrial length may not be solely attributed to its regulation of ER-mitochondrial MCSs since the latter also promotes mitochondrial fusion [36].

Eventually, we examined the role of CHMP7 in mitochondria respiratory function by measuring oxygen consumption rate (OCR). Interestingly, CHMP7 depletion did not affect the basal OCR, but substantially reduced maximal OCR after FCCP injections in both CHMP7-KO HEK293 cells and siRNA-mediated CHMP7-depleted COS7 cells, suggesting an important role of CHMP7 in the fitness of mitochondrial network.

## DISCUSSION

In this manuscript, we identified a previously uncharacterized role of CHMP7 in regulating three-way ER and ER-mitochondria junctions (Fig. 8). Two important questions are still unanswered. First, it is technically challenging to image the ER, mitochondria, and their contacts relative to CHMP7 in mitosis, and thus, the roles of CHMP7 in these ER contacts during mitosis are still unknown. Second, the relationship between mitochondrial dynamics and 3-way ER junctions is still unclear. These questions warrant further investigation.

CHMP7 was suggested to be autoinhibited through the interactions between NT and CT domain, which could be released by LEM2 during the reformation of the NE [27]. Surprisingly, we found that purified GST-CHMP7 directly bound to His-CHMP7 or His-CHMP7-CT in the absence of LEM2. Besides, LEM2-binding defective CHMP7 mutants could still oligomerize (Fig. 8C), and could form puncta at ER contacts (data not shown). These results suggested that the level of CHMP7 oligomerization at the ER contacts may not require the activation of CHMP7 by phase separation of LEM2 [27].

How is CHMP7 oligomerization regulated? Since our results showed that hydrophobic interactions were responsible for CHMP7 oligomerization independently of LEM2, we envisioned that it may be regulated by phosphorylation/dephosphorylation. Future investigations are required to test this hypothesis. In addition, the assembly of CHMP7 at these ER

contacts is mediated by multiple conserved hydrophobic residues in  $\alpha$  helix-2, suggesting that the interactions are multivalent, i.e., one CHMP7 can bind to two or more other CHMP7 molecules. Therefore, both trans and cis interactions among CHMP7 molecules may exist to ensure efficient oligomerization at contacts.

The way that CHMP7 functions at contacts resembles two large GTPases, ATLS or MFN2, respectively. ATLS are suggested to mediate the tethering and/or fusion of ER tubules through trans and cis interactions between ATLS molecules [9]. ATLS inhibition leads to long and unbranched tubules and even disrupted ER tubules [11], and GFP-CHMP7 could partially restore the ER defects resulted from ATLS inhibition, suggesting that CHMP7 may function in parallel with ATLS in the tethering stage. It is still elusive whether CHMP7 plays a role in the fusion of ER tubules. Functionally, ATLS inhibition also caused defects in mitochondrial division in *C. elegans* sensory neuron [37]. Meanwhile, CHMP7 shared similarities with MFN2. First, these two proteins localized to similar cellular compartments, including the ER, the OMM, and MAMs [20]. Second, CHMP7 and MFN2 act at ER contacts in a similar way. MFN2 on the OMM interact in trans either with MFN2 on the other OMM to mediate OMM fusion at the expense of GTP hydrolysis [38], or with MFN2 on the ER to tether mitochondria to the ER [20].

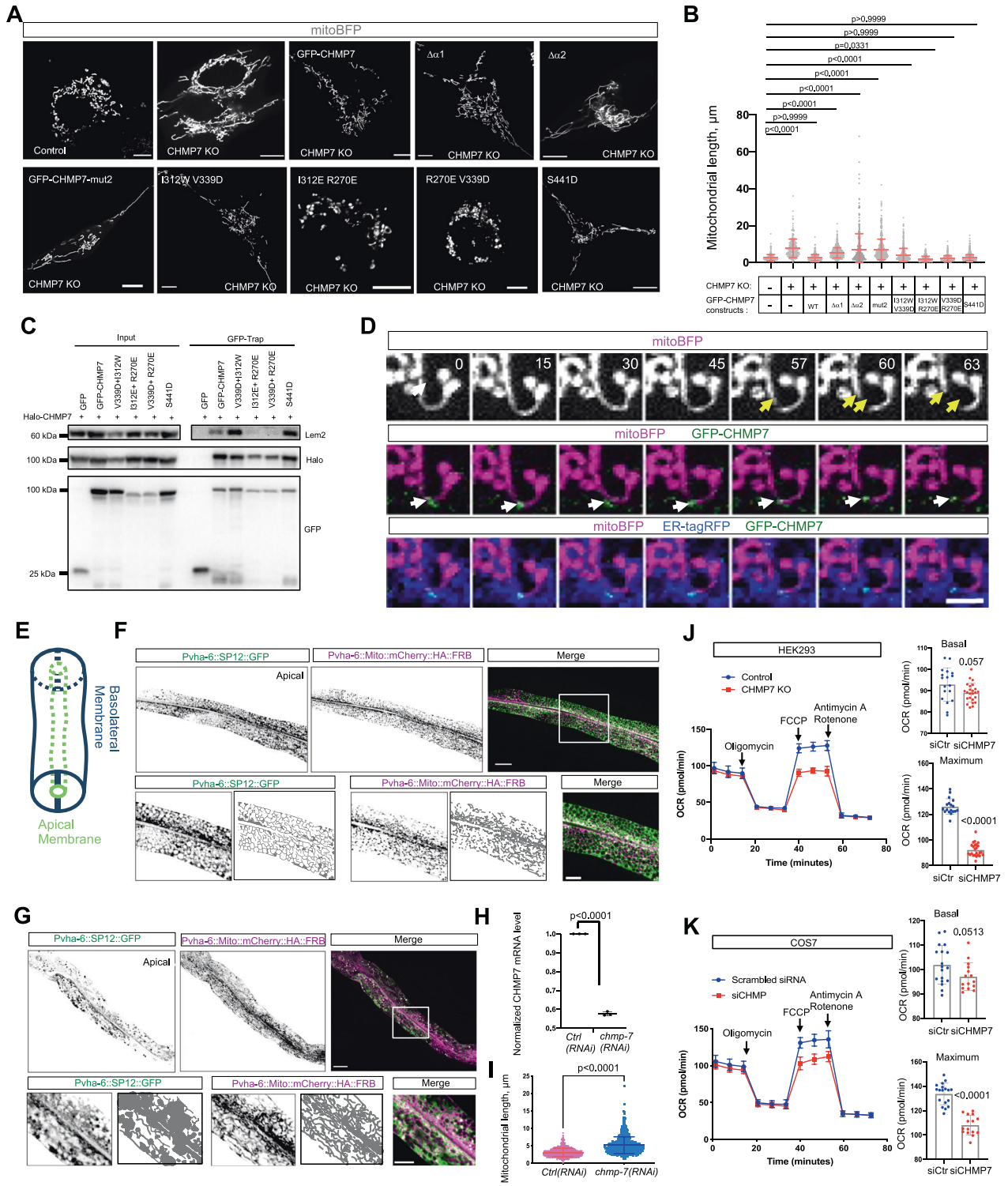
The ER, mitochondria, and MAMs were directly linked to multiple neurodegenerative diseases [39–42], which raised an important question of whether CHMP7 is implicated in the pathology of these diseases. Interestingly, CHMP7 was mainly expressed in the brain and testes, further suggesting a physiological relevance of CHMP7 in these diseases. Supporting this notion, we showed that CHMP7 not only regulated the dynamics of the ER, mitochondria and their interactions, but was required for proper mitochondrial respiratory function. Indeed, a recent study reported that CHMP7 was implicated in familial and sporadic amyotrophic lateral sclerosis (ALS) [43]. Thus, our findings may provide new mechanistic insights for the pathology of this disease.

## MATERIALS AND METHODS

### Cell culture, transfection, stable lines and Crispr-cas9 mediated Halo KI cell lines

African green monkey kidney fibroblast-like COS7 cell line (ATCC), human osteosarcoma U2OS cells (ATCC), human embryonic kidney 293 T (ATCC), and human cervical cancer HeLa cells (ATCC) were grown in DMEM (Invitrogen) supplemented with 10% fetal bovine serum (Gibco) and 1% penicillin/streptomycin. All of the cell lines used in this study are free of mycoplasma contamination.





For transfection, cells were seeded at  $4 \times 10^5$  cells per well in a 6-well dish 16 h before transfection. Plasmid transfections were performed in OPTI-MEM (Invitrogen) with 4  $\mu$ L PEI to each  $\mu$ g plasmid for 5 h, followed by trypsinization, and then replating cells onto glass-bottom confocal dishes at  $3.5 \times 10^5$  cells per well. Cells were imaged in live-cell medium (DMEM with 10%FBS and 20 mM Hepes no P/S)  $\sim$ 16–24 h after transfection. For all transfection experiments in this study, the following amounts of DNA were used per 3.5 cm well (individually or combined for cotransfection): 500 ng for CHMP7 mutations; 700 ng for mito-BFP; 1000 ng for ER-tagRFP and ATLS. For siRNA transfections, cells were plated on 3.5-cm dishes at 30–40% density, and 2  $\mu$ L Lipofectamine RNAiMax

(Invitrogen) and 50 ng siRNA were used per well. At 48 h after transfection, a second round of transfection was performed with 50 ng siRNAs. Cells were analyzed 24 h after the second transfection for depletion.

To generate the Tet-on GFP-CHMP7 COS7 cell line, 293 T cells were seeded into a 10-cm dish with  $3 \times 10^5$  cells 18 h before transfection. Transfections were performed with 4  $\mu$ g Tet-on GFP-CHMP7 constructs, 3  $\mu$ g psPAX2 and 2  $\mu$ g pMD2.G. On the other hand, COS7 cells were seeded onto 10-cm dishes with  $2 \times 10^6$  cells per dish. The supernatant from transfected 293 T cells were collected 48 h after transfection, followed by filtration through a syringe with 0.22  $\mu$ m filter. Then, 1 mL of filtered 293 T supernatant was added to the COS7 cells. COS7 cells were selected in puromycin-containing (1  $\mu$ g/mL)

**Fig. 7 CHMP7 affects mitochondrial division.** **A** Representative images of control and CHMP7 KO HEK293 cells expressing GFP empty vectors, Tet-on GFP-CHMP7 (0.5 ug/ml; 6 h), or Tet-on GFP-CHMP7 mutants (0.5 ug/ml; 6 h) and mitoBFP (gray). **B** Quantification of mitochondrial length from more than 3 independent experiments. Ordinary one-way ANOVA with Tukey's multiple comparisons test. Mean  $\pm$  SD. **C** GFP-Trap assays show that the interactions between GFP-CHMP7 or its mutants and LEM2. **D** Time-lapse images of a COS7 cell expressing Tet-on GFP-CHMP7 (0.5 ug/ml; 6 h; green), ER-tagRFP (blue), and mitoBFP (magenta) with yellow arrows denoting the site of mitochondrial division while white arrows indicating the presence of GFP-CHMP7 punctae at the division site. **E** A diagram of *C. elegans* intestine. **F, G** Representative images of control (**F**) and CHMP7 RNAi (**G**) in *C. elegans* stably expressing intestine-specific SP12-GFP (green; an ER marker) and mito-mCherry-HA-FRB (magenta; a mitochondrial marker) with boxed regions at bottom. **H** Efficiency of CHMP7 depletion by qPCR. Two-tailed unpaired Student's *t* test. Mean  $\pm$  SD. **I** Quantification of mitochondrial length in control ( $n = 947$  mitochondria) and CHMP7 RNAi worms ( $n = 860$  mitochondria). Two-tailed unpaired Student's *t* test. Mean  $\pm$  SEM. **J, K** Mitochondrial oxygen consumption rate (OCR) measured in control and CHMP7-KO HEK293 cells (**J**) or scrambled and CHMP7 siRNA-treated COS7 cells (**K**). OCR trace was obtained by sequential measurement of basal OCR, OCR after the addition of Oligomycin, FCCP, and Rotenone/Antimycin A from 4-6 independent assays. unpaired student's *t*-test. Mean  $\pm$  SD. Scale bar, 10  $\mu$ m in (**A**); 2  $\mu$ m in (**D**); 20  $\mu$ m in big images and 5  $\mu$ m in enlarged images in (**F, G**). Time in sec.

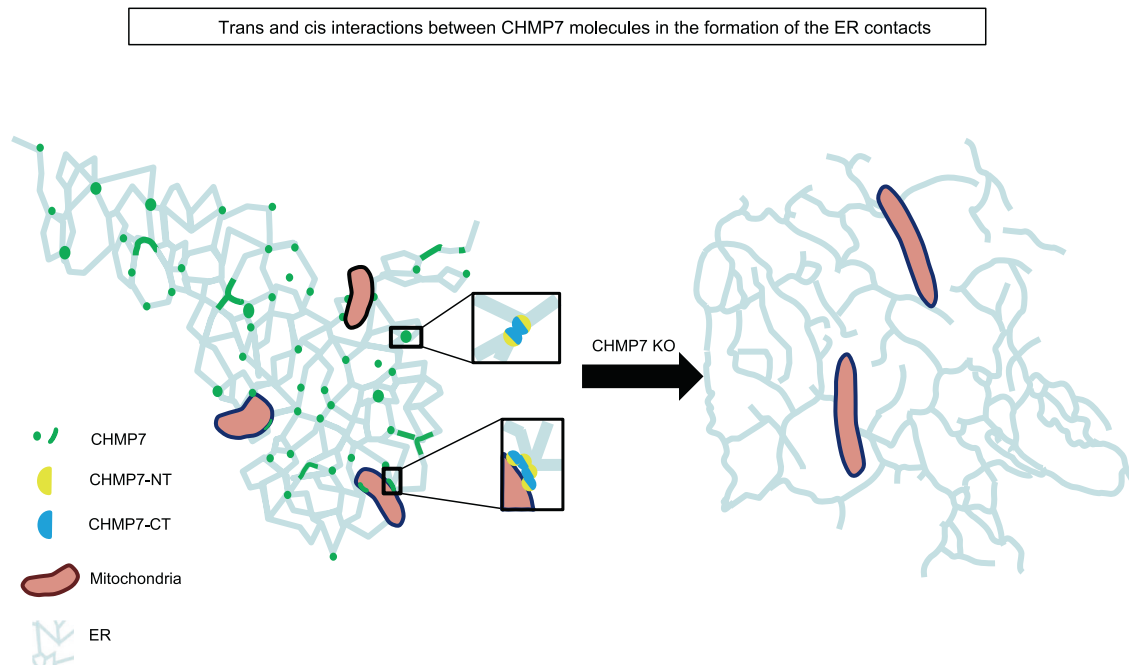


**Fig. 8 The working model of CHMP7 at ER contacts.** CHMP7 localizes to multiple cellular membranes: the ER, MAMs, and the OMM via its NT domain. The localization of CHMP7 at three-way ER and ER-mitochondrial MCSs is determined by hydrophobic interactions among the second  $\alpha$  helix of its CT domain. The dynamic assembly of CHMP7 oligomer regulates the ER morphology and the ER contacts with itself and with mitochondria independently of ESCRT complex. Our results suggest that trans and cis interactions between CHMP7 molecules mediates in the formation of these ER contacts.

medium, and cells were then verified by imaging and western blots. For induction, different amounts of DOX were added to medium 12 h prior to imaging or western blots. To make the CHMP7 KO HEK293 cells and Halo-CHMP7 knock-in RPE1 cell by CRISPR/Cas9, we used the GeCKO system. The donor plasmid contained Halo flanked by  $\sim$ 850 bases upstream of Halo insertion site and  $\sim$ 850 bases downstream. Two guide RNAs (CHMP7-sgRNA1: 5'-CAAGGCTGCGAACACAAGCC-3' and CHMP7-sgRNA2: 5'-TGGGGTCCGATGTGGTCCC-3') were designed for CHMP7 using the CRISPR RGEN website program with PAM site underlined. Donor and guide plasmids were transfected into cells at a 3:1 molar ratio using Lipofectamine 2000 (Invitrogen). Cells were grown in puromycin-containing (0.5  $\mu$ g/mL) medium for 3 days, and Halo positive single cell clones were selected by FACS and single-cell cloned, then verified by sequencing and Western blot (Fig.S2). Donor-only transfected cells were used as negative control. Similar procedures were performed to make CHMP7 KO HEK293 cells, except for the omission of the donor construct.

### C. elegans strains

The *C. elegans* strains were cultured at 20  $^{\circ}$ C on nematode growth medium plates with *Escherichia coli* strain OP50 as the food source. RNAi-mediated interference was performed by feeding the *C. elegans* strains with *E. coli* strain HT115 carrying the L4440 vector expressing double-stranded RNA. If

not specifically indicated in the RNAi experiments, animals in the adult stage were cultured, and the next generation was scored at the day 1 adult stage. The monoclonal colony of HT115 was inoculated in LB medium containing antibiotics, and amplified at 37  $^{\circ}$ C overnight. The bacteria solution was inoculated to nematode growth media plates containing antibiotics and 1 mM IPTG, and leave it at room temperature overnight.

REAGENT or RESOURCE	Source	Catalog NO.
anti-CHMP7	ABclonal	A14360
anti-GFP	ABclonal	AE011
anti-Halo	Promega	G921A
anti-Flag	Sigma	F1804
anti-LEM2	Sigma	HPA017340
anti-Drp1	CST	8570 S
anti-MFN2	Proteintech	12186-1-AP
anti-Mff	Proteintech	17090-1-AP
anti-Calnexin	ABclonal	A15631



REAGENT or RESOURCE	Source	Catalog NO.
anti-VDAC	Abclonal	A0810
anti-Tom20	Santa Cruz	sc17764
anti-VAPB	Proteintech	14477-1-AP
anti-GRP75	Abclonal	A0558
anti-His	Proteintech	66005-1-Ig
anti-actin	Abclonal	AC026
anti-tubulin	Sino Biological Inc	100109-MM05T
anti-GAPDH	Abcam	AB9485
anti-coxIV	Proteintech	11242-1-AP
anti-CyclinB1	Santa Cruz	SC245
anti-LAMP1	CST	9091
anti-Plin2	Abclonal	A6276
anti-TGN46	Abclonal	A19618
anti-rab5A	Proteintech	11947-1-AP

Plasmid	Source
mGFP-C1	Addgene 54579
pCW57-MCS1-P2A-MCS2 (Neo)	Addgene 89180
pLentiCrisprv2	Addgene 52961
mGFP-CHMP7	in this study
mGFP-CHMP7-NT(1-238aa)	This study
mGFP-CHMP7-CT (239-453aa)	This study
mGFP-CHMP7-Δα1	This study
mGFP-CHMP7-Δα2	This study
mGFP-CHMP7-α1-2	This study
mGFP-CHMP7-α3-6	This study
mGFP-CHMP7-α1	This study
mGFP-CHMP7-α2	This study
Tet-on mGFP-CHMP7	This study
Halo-CHMP7	This study
CHMP7-Flag	This study
GST-CHMP7	This study
GST-CHMP7-CT (239-453aa)	This study
14*His-NEDD8-CHMP7	This study
14*His-NEDD8-CHMP7-CT (239-453aa)	This study
3*Flag-GFP nanobody/RFP nanobody	Synthesized by Augct.cn
CHMP7-CT-3*Flag-GFP nanobody/RFP nanobody	This study
Halo-CHMP7-KI	This study
Halo-ATL1	This study
Halo-ATL3	This study
Lnp-Halo	This study

siRNA	Source
siRNA Human CHMP7#1:	Ribobio
5'-GGAGGTGATCGTCTGTAT-3'	
siRNA Human CHMP7#2:	Ribobio
5'-CAAGTCTCTCCAGTCAA-3'	
siRNA Human CHMP7#3:	Ribobio
5'-GAGTGAACAGCTTCTCTCA-3'	
siRNA Human LEM2#1:	Ribobio
5'-GCACTGACCTGGATACTGA-3'	

siRNA	Source
siRNA Human LEM2#2:	Ribobio
5'-GGAGCGCTATCCATATGTA-3'	
siRNA Human LEM2#3:	Ribobio
5'-TGACGACTGTGGACAAGGT-3'	
siRNA Human ATL2#1:	Synthesized by Augct.cn
5'-UCCUGGUCUAAAGUUGCAACUAAU-3'	
siRNA Human ATL2#2:	Synthesized by Augct.cn
5'-GAGAGCUUCGAAAUCUGGUUCAUU-3'	
siRNA Human ATL3#1:	Synthesized by Augct.cn
5'-GCCUGACUUUGAUGGGAAUUAAA-3'	
siRNA Human ATL3#2:	Synthesized by Augct.cn
5'-GGGCUACAUCAGUUAUUCUGGUCAA-3'	
siRNA Human CHMP1B#1:	Ribobio
5'-GGAGCAGGATGAAGTCTCT-3'	
siRNA Human CHMP1B#2:	Ribobio
5'-GGCGGTGAATTTCTTGAGA-3'	
siRNA Human CHMP1B#3:	Ribobio
5'-CATGGAAGTTGCGAGGATA-3'	
siRNA Human CHMP4B#1:	Ribobio
5'-GACGGCATTATCAACCA-3'	
siRNA Human CHMP4B#2:	Ribobio
5'-GGACATCGATAAAGTTGAT-3'	
siRNA Human CHMP4B#3:	Ribobio
5'-GGCGGAATTAGAAGAACTA-3'	
siRNA Human CHMP6#1:	Ribobio
5'-TCACCCAGATCGAAATGAA-3'	
siRNA Human CHMP6#2:	Ribobio
5'-TGCTCAAGAAGAAGCGATA-3'	
siRNA Human CHMP6#3:	Ribobio
5'-GCTTCACTCAGGAGGATGA-3'	
siRNA Human TSG101#1:	Ribobio
5'-GAATCTGTATGCAGAAGAA-3'	
siRNA Human TSG101#2:	Ribobio
5'-GGTTACCCGTTTAGATCAA-3'	
siRNA Human TSG101#3:	Ribobio
5'-CCACAACAAGTCTCAGTA-3'	
siRNA Human VPS4A#1:	Ribobio
5'-CCAGCATGATGATTGATGA-3'	
siRNA Human VPS4A#2:	Ribobio
5'-GATGGAGAAGCCCAACATA-3'	
siRNA Human VPS4A#3:	Ribobio
5'-GGAGATGACTTGGATGGAT-3'	
siRNA Human VPS28#1:	Ribobio
5'-GACGAATTCTGCCGCAAGT-3'	
siRNA Human VPS28#2:	Ribobio
5'-GCTCCTGGTCCAATACAAA-3'	
siRNA Human VPS28#3:	Ribobio
5'-CTCAGAAATCAGCTCTATT-3'	
siRNA Human ALIX #1:	Ribobio
5'-GAAGGATGCTTCGATAAAA-3'	

siRNA	
siRNA Human ALIX #2:	Ribobio
5'-GGCACAGGCTCAAGAAGTA-3'	
siRNA Human ALIX #3:	Ribobio
5'-GAACCTGGATAATGATGAA-3'	
siRNA Human IST1#1:	Ribobio
5'-AGAGACAGATCTTATTGAT-3'	
siRNA Human IST1#2:	Ribobio
5'-CCAGACCTGCAGATAACTA-3'	
siRNA Human IST1#3:	Ribobio
5'-GACATTAATGCTGATAAGA-3'	
siRNA Human scrambled siRNA	Ribobio
5'-CGUUAUUCGCUAAUUAUACGCUAT-3'	
Primers	Sequences (5'-3')
mGFP-CHMP7-F	gcttcgaattctcagtcgacATGTGGTCCCCGGAGCGG
mGFP-CHMP7-R	cggtggatccgggcccggCTACAATGGCTTTAGAGTCGGTTCC
mGFP-CHMP7-NT(1-238aa)-F	gcttcgaattctcagtcgacATGTGGTCCCCGGAGCGG
mGFP-CHMP7-NT(1-238aa)-R	ttatctagatccggtgatccTTAATCTACGTCTTACTGACTGGAGAGAC
mGFP-CHMP7-CT(239-453aa)-F	gcttcgaattctcagtcgacATGGTTGGGTGTACCAGCTG
mGFP-CHMP7-CT(239-453aa)-R	ttatctagatccggtgatccCTACAATGGCTTTAGAGTCGGTTCC
mGFP-CHMP7-Δα1-F	tgacgtagatAAGCAGCTGGCACTGAGGTC
mGFP-CHMP7-Δα1-R	ccagctgcttATCTACGTCTTACTGACTGGAGAGACC
mGFP-CHMP7-Δα2-F	aaagGTGGAGAAGGCAGAGAGCCTC
mGFP-CHMP7-Δα2-R	ttctctcctcccaCTTTCCTGCTCGGCATGCC
mGFP-CHMP7-α1-2-F	gcttcgaattctcagtcgacATGGTTGGGTGTACCAGCTG
mGFP-CHMP7-α1-2-R	cggtggatccgggcccggTCATGTGACATCCTCATGGAGA
mGFP-CHMP7-α3-6-F	gcttcgaattctcagtcgacATGGTTGGAGAAGGCAGAGAGC
mGFP-CHMP7-α3-6-R	cggtggatccgggcccggCTACAATGGCTTTAGAGTCGGTTCC
mGFP-CHMP7-α1-F	gcttcgaattctcagtcgacATGGTTGGGTGTACCAGCTG
mGFP-CHMP7-α1-R	cggtggatccgggcccggCTACTTCTGCTCGGCATGC
mGFP-CHMP7-α2-F	gcttcgaattctcagtcgacATGAAGCAGCTGGCACTGAGG
mGFP-CHMP7-α2-R	cggtggatccgggcccggTCATGTGACATCCTCATGGAGA
Tet-on mGFP-CHMP7-F	tcgctggagaattgctagcATGGTGAGCAAGGGCGAGG
Tet-on mGFP-CHMP7-R	gttgctgctccggaacggctTACAATGGCTTTAGAGTCGGTTCC
Halo-CHMP7-F	ctggagattccctcagctcATGTGGTCCCCGGAGCGG
Halo-CHMP7-R	gtaccgtcagctcagaattCTACAATGGCTTTAGAGTCGGTTCC
CHMP7-Flag-F	tcgagctcaagctcgaattcATGTGGTCCCCGGAGCGG
CHMP7-Flag-R	tttgaatcacgggtgatccCAATGGCTTTAGAGTCGGTTCC
GST-CHMP7-F	gatctggttccgctggtatccATGTGGTCCCCGGAGCGG
GST-CHMP7-R	tcagtcagtcacgatgaattCTACAATGGCTTTAGAGTCGGTTCC
GST-CHMP7-CT (239-453aa)-F	gatctggttccgctggtatccATGTGGTGGGTGTACCAGCTG
GST-CHMP7-CT (239-453aa)-R	tcagtcagtcacgatgaattCTACAATGGCTTTAGAGTCGGTTCC
14*His-NEDD8-CHMP7-F	ggcgccggtactcgggatccATGTGGAGCCCCGAGAGAGA
14*His-NEDD8-CHMP7-R	gctcagctaattaagaagcttCACAGGGGCTTCAGGGTG
14*His-NEDD8-CHMP7-CT (239-453aa)-F	ggcgccggtactcgggatccATGTGGTGGGTGTACCAGCTG
14*His-NEDD8-CHMP7-CT (239-453aa)-R	gctcagctaattaagaagcttCTACAATGGCTTTAGAGTCGGTTCC

Primers	Sequences (5'-3')
CHMP7-CT-3*Flag-GFP nanobody-F	gCTTCgAATTCTgCAgTCgACgCCACCATggTTggggTgTACCgCTg
CHMP7-CT-3*Flag-GFP nanobody-R	CggTggATCCCgggCCCGgCggCAATggCTTTAgAgTCggTTCC
CHMP7-CT-3*Flag-RFP nanobody-F	TgAACCGTCAgATCCgCTAgCgCCACCATggTTggggTgTACCgCTg
CHMP7-CT-3*Flag-RFP nanobody-R	TAATCCATggTggCgACCCggCAATggCTTTAgAgTCggTTCC
CHMP7 LHA-F	tataagcttctctgtgtgttttggcagagtggtcttcaagaatgtgtcc
CHMP7 LHA-R	tatgaattcCGGAACCCAGCCCCGGCAAGGCTCGGAACACAAGCCTGaC
Halo-F	gataagcttgatcatgaattcGCCACCATGgaaatcggtagctgttccat
Halo-R	CGGGGACCACATACCGTGGaaatccagagtagacagacca
CHMP7 RHA-F	AgatttccACCCGGTATGTGGTCCCCGGAGCGG
CHMP7 RHA-R	cgaattggagctccaccggtgatcatgtattgatatacaatgttacctc
Halo-ATL1-F	atttccctcagctcaagcttATGGCCAAGAACCAGCGG
Halo-ATL1-R	ttatctagatccggtgatccTTACATTTTTTTCTTTCTGATTGTCA
Halo-ATL3-F	atttccctcagctcaagcttATGGTTCCTCCAGCAGGAGTG
Halo-ATL3-R	ttatctagatccggtgatccCTATTGAGCTTTTTATCCATGGATG
Lnp-Halo-F	tcgagctcaagctcgaattcATGGGTGGATTATTTCTCGATG
Lnp-Halo-R	cggtggatccgggcccggCTCTGCCGCAAGATTCTCCA
CHMP7 KI sgRNA-1	CAAGGCTCGGAACACAAGCC
CHMP7 KI sgRNA-2	TGGGGTTCGATGTGGTCCC

### Live imaging by confocal microscopy

Cells were grown on glass-bottom confocal dishes. Confocal dishes were loaded to a laser scanning confocal microscope (LSM780, Zeiss, Germany) equipped with multiple excitation lasers (405 nm, 458 nm, 488 nm, 514 nm, 561 nm, 633 nm) and spectral fluorescence GaAsP array detector. Cells were imaged with the 63 × 1.4-NA iPlan-Apochromat 63x oil objective using the 405-nm laser for BFP, 488-nm for GFP, 561-nm for mStrawberry, OFF, tagRFP or mCherry.

For tracking the dynamics of the ER and mitochondria, cells on confocal dishes were loaded to a spinning disc confocal microscope (Olympus IX83, Japan) equipped with 100x/1.4 oil (WD 013 mm, DIC slider) objective, multiple lasers (405 nm, 488 nm, 561 nm, and 640 nm) with corresponding filters and EMCCD and sCMOS cameras.

### Live-cell high-resolution confocal imaging

Cells on confocal dishes were loaded to a laser scanning confocal microscope (A1si, Nikon) equipped with multiple excitation lasers (405 nm, 488 nm, 561 nm, 640 nm) and corresponding filters. Cells were imaged with 405-nm laser for BFP, 488-nm for GFP, 561-nm for OFF, tagRFP or mCherry and 640-nm for Janelia Fluor 646 HaloTag Ligand. Cells on confocal dishes were loaded to a laser scanning confocal microscope (Leica STELLARIS 5) equipped with multiple excitation lasers (405 nm, 499 nm, 533 nm) and 63X/1.40 IL, under control of LAS X software.

### Immunofluorescence staining

Cells were fixed with 4% PFA (paraformaldehyde, Sigma) in PBS for 10 min at room temperature. After washing with PBS three times, cells were permeabilized with 0.1% Triton X-100 in PBS for 15 min on ice. Cells were then washed three times with PBS, blocked with 0.5% BSA in PBS for 1 h, incubated with primary antibodies in diluted blocking buffer overnight, and washed with PBS three times. Secondary antibodies were applied for 1 h at room temperature. After washing with PBS three times, samples were mounted on Vectashield (H-1000; Vector Laboratories).

### Oxygen consumption rate (OCR) measurements using Seahorse XF Cell Mito Stress Test

The day before the experiment, prewarm XF Calibrant and hydrate a sensor cartridge in sterile water at 37 °C in a non-CO<sub>2</sub> incubator overnight.



HEK293 cells or Cos-7 cells were seeded in XF96 Cell Culture Microplate in normal growth medium about 18 h before transfection. The day of the experiment, hydrate a sensor cartridge in prewarmed XF Calibrant at 37 °C in a non-CO<sub>2</sub> incubator 45–60 min. Prepare Standard Substrate Oxidation Stress Test assay media by supplementing with 10 mM glucose, 1 mM pyruvate, 2 mM glutamine, adjust pH to 7.4 and warm media to 37 °C. Remove the growth medium from the cell culture microplate. Wash once with warmed assay medium. Add assay medium to a final volume of 180 µl/well for 96-well plates. Incubate cell plates with assay medium at 37 °C in a non-CO<sub>2</sub> incubator for 45–60 min prior to the assay. Meanwhile, the assay cartridge was loaded with XF Cell Mito Stress Test compounds (final concentrations: 1.5 µM oligomycin, 1 µM FCCP, 0.5 µM rotenone, and 0.5 µM antimycin A). Then the XF Cell Culture Microplate was inserted into the XFe96 Analyzer and run the XF Cell Mito Stress Test according to the manufacturer's instructions.

### Duolink PLA fluorescence protocol

Cells were fixed with 4% PFA (paraformaldehyde, Sigma) in PBS for 20 min at room temperature. After washing with PBS three times, cells were permeabilized with 0.5% Triton X-100 in PBS for 10 min on ice. Cells were then washed three times with PBS, blocked with Duolink Blocking Solution for 1 h at 37 °C. Dilute primary antibodies in the Duolink Antibody Diluent and incubated overnight at 4 °C. Wash the slides 2 × 5 min in 1x Wash Buffer A at room temperature and apply the PLA probe solution for 1 h at 37 °C. Wash the slides 2 × 5 min in 1x Wash Buffer A at room temperature and apply the ligation solution for 30 min at 37 °C. Wash the slides 2 × 5 min in 1x Wash Buffer A at room temperature and apply the amplification solution for 100 min at 37 °C. Wash the slides 2 × 10 min in 1x Wash Buffer B at room temperature. Wash the slides in 0.01x Wash Buffer B for 1 min. Samples were mounted on Mounting medium with DAPI.

### Image analysis

All image analysis and processing were performed using ImageJ (National Institutes of Health). Colocalization-based analysis of ER-mitochondrial contacts was performed by colocalization plugin (imageJ, NIH) with the following settings: Ratio (0–100%): 50; Threshold channel 1 (0–255): 50; Threshold channel 2 (0–255): 50; Display value (0–255): 255. ER-mitochondria intersection sites were automatically identified by colocalization plugin with white pixels representing potential ER-mitochondrial contact sites. For mitochondrial perimeter measurement, an imageJ macro named mitochondrial morphology macro0 [44] was used to measure the perimeter of mitochondria in region of interests (ROIs) where mitochondria are well resolved.

### Isolation of MAMs from mouse brain and HEK293 cells

Three mouse brains were used in the experiment. Three male C57BL/6 mice (age, 10 weeks; weight, 25–30 g) were euthanized and the brains were harvested quickly. Half of the brain were taken into a pre-chilled tubes and got weighed. The following procedures demonstrate the treatment of a half of a brain. A half brain was ground in a tissue grinder containing 1 mL cold solution A (0.32 M Sucrose, 1 mM NaHCO<sub>3</sub>, 1 mM MgCl<sub>2</sub>, 0.5 mM CaCl<sub>2</sub>, Protease Inhibitors cocktail) for 15 times. The lysate was diluted to 10x volumes w/v (e.g., 0.248 g to 2.48 mL) and centrifuged at 1400 × g for 10 min at 4 °C, followed by transferring the supernatant to a 50 mL tube. The pellet was then resuspended with 10x volumes of solution A and ground for 5 times, and mixture was then centrifuged at 710 × g for 10 min at 4 °C. The pellet mainly containing the nuclei and cell debris were removed, and the supernatant was centrifuged at 13,800 × g for 10 min at 4 °C. The supernatant was transferred to a 50 mL tube on ice, and the pellet was resuspended with 10x volumes of solution A, and ground for 5 times, and then centrifuged at 13,800 × g for 10 min at 4 °C. This above step was repeated for once. Subsequently, the supernatant (cytosol and ER) was pooled and kept on ice, where the resulting pellet contained mitochondrial fraction.

Next, the pellet was resuspended in 4.8 mL/g of Solution B (0.32 M Sucrose, 1 mM NaHCO<sub>3</sub> + Protease Inhibitors), and ground for 6 times, loaded to sucrose gradients containing 0.32 M, 0.85 M, 1 M, and 1.2 M sucrose, before centrifugation at 82,500 × g for 2 h at 4 °C. This resulted in three bands and a pellet: (1) 0.32–0.85 M interface: myelin and other membrane contaminants; (2) 0.85–1 M interface: ER, Golgi, plasma membranes; (3) 1–1.2 M interface: synaptosome; (4) pellet: crude mitochondria. The freshly isolated crude mitochondria were resuspended with Isolation Medium (250 mM Mannitol, 5 mM Hepes pH 7.4, 0.5 mM EGTA, 0.1% BSA) containing freshly added protease inhibitors. Then, mitochondrial

suspension was loaded on top of 30% Percoll gradient with Gradient Buffer (final concentration: 225 mM Mannitol, 25 mM Hepes pH 7.5, 1 mM EGTA, 0.1% BSA) in an Ultra-Clear Beckman Centrifuge Tube, and centrifuged at 95,000 × g for 30 min, 4 °C. The heavy fraction (lower band) was transferred to a fresh round-bottom glass tube on ice, and the light fraction (upper band) was transferred to a separate fresh round-bottom glass tube on ice. Both fractions were diluted with 10 mL Isolation Medium and centrifuged at 6300 × g for 10 min at 4 °C. The supernatant from the heavy fraction was removed, and the pellet was resuspended with another 10 mL Isolation Medium and centrifuged again at 6300 × g for 10 min at 4 °C. The resulting pellet contained the pure mitochondrial fraction. Finally, the supernatant from the light fraction was transferred to an Ultra-Clear Beckman Centrifuge Tube, filled up with sufficient Isolation Medium and centrifuged at 100,000 × g for 1 h at 4 °C. The resulting pellet contained the MAMs fraction.

For MAM preparation from HEK293 cells, 200 mL of HEK293 cells in a density of ~2 × 10<sup>6</sup> /mL were transfected with GFP-CHMP7 or GFP-CHMP7-mut2. Cells were lysed by sonication 72 h after transfection. The following steps were similar as the procedures in the preparation of MAMs from mouse brain.

### Differential centrifugation

Differential centrifugation was performed with a protocol previously described [34], with modifications. Cells were harvested from 2 × 10 cm dishes at 90% confluency. The following steps were conducted at 4 °C or on ice. Cells were washed with pre-cold PBS twice and homogenized in isolation buffer (225 mM mannitol, 75 mM sucrose, 0.1 mM EGTA, 30 mM Tris-HCl pH 7.4) by Dounce (Wheaton Dura-Grind). The homogenate was centrifuged at 600 × g for 10 min twice to remove the nuclei and debris. The resulting supernatant was centrifuged for 15 min at 13,000 × g three times to obtain crude mitochondria. Western blot was performed using rabbit anti-VAPB (1:1000, 14477-1-AP, ProteinTech), rabbit anti-Calnexin (1:1000, 10427-2-AP, ProteinTech), and rabbit anti-VDAC (1:1000, 10866-1-AP, ProteinTech).

### Electron microscopy

Tet-on GFP-CHMP7 COS cells with (1 µg/mL, 12 h) or without Dox treatments were fixed with 2.5% glutaraldehyde in 0.1 M Phosphate buffer, pH 7.4 for 2 h at room temperature. After washing three times with 0.1 M Phosphate buffer, cells were scraped and collected with 0.1 M phosphate buffer followed by centrifugation at 3,000 rpm. The pellet was resuspended in PBS (0.1 M), and centrifuged at 3,000 rpm for 10 min. This step was repeated for three times. The samples were post-fixed with pre-cold 1% OsO<sub>4</sub> in 0.1 M Phosphate buffer for 2–3 h at 4 °C, followed by rinsing with PBS 3 times (3 × 20 min). The samples were dehydrated in graded ethanol (50%, 70%, 85%, 90%, 95%, 2 × 100%) with 15 min for each condition. The penetrations were performed in an order of acetone-epoxy (2:1); acetone-epoxy (1:1); epoxy. Each round of penetration was performed at 37 °C for 12 h. The samples were embedded in epoxy resin using standard protocols [45]. Sections parallel to the cellular monolayer were obtained using a Leica EM UC7 with the thickness of 60–100 nm and examined under Tecnai G2 20 TWIN (FEI) with accelerating voltage 200 kv. Mitochondria and ER were identified based on their respective morphology and were traced by hand. The extension length of ER-mitochondrial contact regions was measured using the “measure” tool in ImageJ (NIH) along ER and mitochondria contact regions. Mitochondria with ER within 30 nm at any point on the mitochondrial circumference were identified as contact sites.

### GFP-trap assay

GFP trap (GFP-trap agarose beads, ChromoTek) was used for detection of protein-protein interactions and the GFP-Trap assays were performed according to the manufacturer's protocol. 5% input was used in GFP traps unless otherwise indicated. Briefly, cells were lysed in Lysis buffer (50 mM Tris-HCl pH 7.5, 150 mM NaCl, 1 mM EDTA, 0.5% Triton, 1x Proteases Inhibitor cocktail, 0.7% N-ethylmaleimide). After incubation of GFP-Trap beads overnight at 4 °C, the beads were pelleted and washed three times with dilution buffer (10 mM Tris-HCl pH 7.5, 150 mM NaCl, 0.5 mM EDTA, 1x Proteases Inhibitor cocktail, 0.7% N-ethylmaleimide).

### Protein expression and purification

GST and His constructs were transformed into Escherichia coli BL21 (DE3) cells, and cells were incubated at 37 °C until the optical density at 600 nm reached 0.6–0.8. Then cells were induced with 1 mM IPTG at 37 °C for 4 h.

GST fusion proteins were purified via the GST-tag Protein Purification kit (P2262, Beyotime). His fusion proteins were purified via Ni-NTA resin (30210, QIAGEN) according to the manufacturer's instructions.

### Statistical analysis

All statistical analyses and *p*-value determinations were performed in GraphPad Prism6. To determine *P*-values, an ordinary one-way ANOVA with Tukey's multiple comparison tests was performed among multiple groups. A two-tailed unpaired Student's *t*-tests was performed between two groups of data. The error bars in plots represented mean  $\pm$  SD unless otherwise stated.

### Reporting summary

Further information on research design is available in the Nature Research Reporting Summary linked to this article.

### DATA AVAILABILITY

The datasets generated during and/or analyzed during the current study are available from the corresponding author on reasonable request.

### REFERENCES

- Baumann O, Walz B. Endoplasmic reticulum of animal cells and its organization into structural and functional domains. *Int Rev Cytol.* 2001;205:149–214.
- English AR, Voeltz GK. Endoplasmic reticulum structure and interconnections with other organelles. *Cold Spring Harb Perspect Biol.* 2013;5:a013227.
- Hu J, Prinz WA, Rapoport TA. Weaving the web of ER tubules. *Cell* 2011;147:1226–31.
- Lee C, Chen LB. Dynamic behavior of endoplasmic reticulum in living cells. *Cell* 1988;54:37–46.
- Waterman-Storer CM, Salmon ED. Endoplasmic reticulum membrane tubules are distributed by microtubules in living cells using three distinct mechanisms. *Curr Biol.* 1998;8:798–806.
- Prinz WA, Toulmay A, Balla T. The functional universe of membrane contact sites. *Nat Rev Mol Cell Biol.* 2020;21:7–24.
- Wu H, Carvalho P, Voeltz GK. Here, there, and everywhere: The importance of ER membrane contact sites. *Science.* 2018;361:eaan5835.
- Hu J, Shibata Y, Zhu PP, Voss C, Rismanchi N, Prinz WA, et al. A class of dynamine-like GTPases involved in the generation of the tubular ER network. *Cell* 2009;138:549–61.
- Liu TY, Bian X, Romano FB, Shemesh T, Rapoport TA, Hu J. Cis and trans interactions between atlastin molecules during membrane fusion. *Proc Natl Acad Sci USA.* 2015;112:E1851–60.
- Wang S, Romano FB, Field CM, Mitchison TJ, Rapoport TA. Multiple mechanisms determine ER network morphology during the cell cycle in *Xenopus* egg extracts. *J Cell Biol.* 2013;203:801–14.
- Wang S, Tukachinsky H, Romano FB, Rapoport TA. Cooperation of the ER-shaping proteins atlastin, lunapark, and reticulons to generate a tubular membrane network. *Elife.* 2016;5:e18605.
- Orso G, Pendlin D, Liu S, Tosetto J, Moss TJ, Faust JE, et al. Homotypic fusion of ER membranes requires the dynamine-like GTPase atlastin. *Nature* 2009;460:978–83.
- Chen S, Desai T, McNew JA, Gerard P, Novick PJ, Ferro-Novick S. Lunapark stabilizes nascent three-way junctions in the endoplasmic reticulum. *Proc Natl Acad Sci USA.* 2015;112:418–23.
- Zhou X, He Y, Huang X, Guo Y, Li D, Hu J. Reciprocal regulation between lunapark and atlastin facilitates ER three-way junction formation. *Protein Cell.* 2019;10:510–25.
- Saheki Y, De Camilli P. Endoplasmic reticulum-plasma membrane contact sites. *Annu Rev Biochem.* 2017;86:659–84.
- Csordas G, Renken C, Varnai P, Walter L, Weaver D, Buttke KF, et al. Structural and functional features and significance of the physical linkage between ER and mitochondria. *J Cell Biol.* 2006;174:915–21.
- Friedman JR, Lackner LL, West M, DiBenedetto JR, Nunnari J, Voeltz GK. ER tubules mark sites of mitochondrial division. *Science.* 2011;334:358–62.
- Eisenberg-Bord M, Shai N, Schuldiner M, Bohnert M. A tether is a tether: tethering at membrane contact sites. *Dev Cell.* 2016;39:395–409.
- Kormmann B, Currie E, Collins SR, Schuldiner M, Nunnari J, Weissman JS, et al. An ER-mitochondria tethering complex revealed by a synthetic biology screen. *Science.* 2009;325:477–81.
- de Brito OM, Scorrano L. Mitofusin 2 tethers endoplasmic reticulum to mitochondria. *Nature* 2008;456:605–10.
- Szabadkai G, Bianchi K, Varnai P, De Stefani D, Wieckowski MR, Cavagna D, et al. Chaperone-mediated coupling of endoplasmic reticulum and mitochondrial Ca<sup>2+</sup> channels. *J Cell Biol.* 2006;175:901–11.
- Iwasawa R, Mahul-Mellier AL, Datler C, Pazarentzos E, Grimm S. Fis1 and Bap31 bridge the mitochondria-ER interface to establish a platform for apoptosis induction. *EMBO J.* 2011;30:556–68.
- De Vos KJ, Morotz GM, Stoica R, Tudor EL, Lau KF, Ackerley S, et al. VAPB interacts with the mitochondrial protein PTPIP51 to regulate calcium homeostasis. *Hum Mol Genet.* 2012;21:1299–311.
- Kumar N, Leonzino M, Hancock-Cerutti W, Horenkamp FA, Li P, Lees JA, et al. VPS13A and VPS13C are lipid transport proteins differentially localized at ER contact sites. *J Cell Biol.* 2018;217:3625–39.
- Gatta AT, Olmos Y, Stoten CL, Chen Q, Rosenthal PB, Carlton JG. CDK1 controls CHMP7-dependent nuclear envelope reformation. *Elife.* 2021;10:e59999.
- Lee IJ, Stokasimov E, Dempsey N, Varberg JM, Jacob E, Jaspersen SL, et al. Factors promoting nuclear envelope assembly independent of the canonical ESCRT pathway. *J Cell Biol.* 2020;219:e201908232.
- von Appen A, LaJoie D, Johnson IE, Trmka MJ, Pick SM, Burlingame AL, et al. LEM2 phase separation promotes ESCRT-mediated nuclear envelope reformation. *Nature.* 2020;582:115–8.
- Olmos Y, Perdrix-Rosell A, Carlton JG. Membrane Binding by CHMP7 Coordinates ESCRT-III-Dependent Nuclear Envelope Reformation. *Curr Biol.* 2016;26:2635–41.
- Horii M, Shibata H, Kobayashi R, Katoh K, Yorikawa C, Yasuda J, et al. CHMP7, a novel ESCRT-III-related protein, associates with CHMP4b and functions in the endosomal sorting pathway. *Biochem J.* 2006;400:23–32.
- Rowland AA, Voeltz GK. Endoplasmic reticulum-mitochondria contacts: function of the junction. *Nat Rev Mol Cell Biol.* 2012;13:607–25.
- Ji WK, Hatch AL, Merrill RA, Strack S, Higgs HN. Actin filaments target the oligomeric maturation of the dynamin GTPase Drp1 to mitochondrial fission sites. *Elife* 2015;4:e11553.
- Niu L, Ma T, Yang F, Yan B, Tang X, Yin H, et al. Atlastin-mediated membrane tethering is critical for cargo mobility and exit from the endoplasmic reticulum. *Proc Natl Acad Sci USA.* 2019;116:14029–38.
- Gao Y, Xiong J, Chu QZ, Ji WK. PDZD8-mediated lipid transfer at contacts between the ER and late endosomes/lysosomes is required for neurite outgrowth. *J Cell Sci.* 2022;135:jcs255026.
- Ji WK, Chakrabarti R, Fan X, Schoenfeld L, Strack S, Higgs HN. Receptor-mediated Drp1 oligomerization on endoplasmic reticulum. *J Cell Biol.* 2017;216:4123–39.
- Otera H, Wang C, Cleland MM, Setoguchi K, Yokota S, Youle RJ, et al. Mff is an essential factor for mitochondrial recruitment of Drp1 during mitochondrial fission in mammalian cells. *J Cell Biol.* 2010;191:1141–58.
- Abrisch RG, Gumbin SC, Wisniewski BT, Lackner LL, Voeltz GK. Fission and fusion machineries converge at ER contact sites to regulate mitochondrial morphology. *J Cell Biol.* 2020;219:e201911122.
- Liu X, Guo X, Niu L, Li X, Sun F, Hu J, et al. Atlastin-1 regulates morphology and function of endoplasmic reticulum in dendrites. *Nat Commun.* 2019;10:568.
- Chen H, Detmer SA, Ewald AJ, Griffin EE, Fraser SE, Chan DC. Mitofusins Mfn1 and Mfn2 coordinately regulate mitochondrial fusion and are essential for embryonic development. *J Cell Biol.* 2003;160:189–200.
- Cali T, Ottolini D, Negro A, Brini M. alpha-Synuclein controls mitochondrial calcium homeostasis by enhancing endoplasmic reticulum-mitochondria interactions. *J Biol Chem.* 2012;287:17914–29.
- Area-Gomez E, Del Carmen Lara Castillo M, Tambini MD, Guardia-Laguarda C, de Groof AJ, Madra M, et al. Upregulated function of mitochondria-associated ER membranes in Alzheimer disease. *EMBO J.* 2012;31:4106–23.
- Filadi R, Greotti E, Turacchio G, Luini A, Pozzan T, Pizzo P. Presenilin 2 modulates endoplasmic reticulum-mitochondria coupling by tuning the antagonistic effect of mitofusin 2. *Cell Rep.* 2016;15:2226–38.
- Hedskog L, Pinho CM, Filadi R, Ronnback A, Hertwig L, Wiehager B, et al. Modulation of the endoplasmic reticulum-mitochondria interface in Alzheimer's disease and related models. *Proc Natl Acad Sci USA.* 2013;110:7916–21.
- Coyne AN, Baskerville V, Zaepfel BL, Dickson DW, Rigo F, Bennett F, et al. Nuclear accumulation of CHMP7 initiates nuclear pore complex injury and subsequent TDP-43 dysfunction in sporadic and familial ALS. *Sci Transl Med.* 2021;13:eabe1923.
- Dagda RK, Zhu J, Kulich SM, Chu CT. Mitochondrially localized ERK2 regulates mitophagy and autophagic cell stress: implications for Parkinson's disease. *Autophagy.* 2008;4:770–82.
- Kumar S, Ciraolo G, Hinge A, Filippi MD. An efficient and reproducible process for transmission electron microscopy (TEM) of rare cell populations. *J Immunol Methods.* 2014;404:87–90.
- Jumper J, Evans R, Pritzel A, Green T, Figurnov M, Ronneberger O, et al. Highly accurate protein structure prediction with AlphaFold. *Nature.* 2021;596:583–9.

### ACKNOWLEDGEMENTS

We thank Ping Liu (the Optical Bioimaging Core Facility of WNLO-HUST), Linfang Yang (Huazhong University of Science and Technology) for imaging assistance, and Wenjun Pu (Shenzhen Bay Laboratory) for technical help with CHMP7 Halo KI.



### AUTHOR CONTRIBUTIONS

QC, JW, YD, TZ, JX, WJ, LD conceived the project and designed the experiments. QC, JW, YD, TZ performed the experiments. QC, JW, YD, TZ, AS, JX, WJ, LD analyzed and interpreted the data. WJ prepared the manuscript with inputs and approval from all authors.

### FUNDING

JX was supported by National Natural Science Foundation of China (81901166). LD was supported by the Guangdong Basic and Applied Basic Research Foundation (2020A1515110542) and Shenzhen Bay Laboratory Open Fund (SZBL2020090501004). WJ was supported by National Natural Science Foundation of China (32122025; 91854109), and the Program for HUST Academic Frontier Youth Team (2018QYTD11).

### COMPETING INTERESTS

The authors declare no competing interests.

### ETHICS APPROVAL

All experimental procedures involving animals were approved by Animal Use and Care Committee of Huazhong University of Science and Technology, Wuhan, China. All animal care and use followed the guidelines of the Animal Care and Use

Committee of Huazhong University of Science and Technology. During all procedures of experiments, the number of animals and their suffering by treatments were minimized.

### ADDITIONAL INFORMATION

**Supplementary information** The online version contains supplementary material available at <https://doi.org/10.1038/s41418-022-01048-2>.

**Correspondence** and requests for materials should be addressed to Juan Xiong, Wei-Ke Ji or Lin Deng.

**Reprints and permission information** is available at <http://www.nature.com/reprints>

**Publisher's note** Springer Nature remains neutral with regard to jurisdictional claims in published maps and institutional affiliations.

Springer Nature or its licensor holds exclusive rights to this article under a publishing agreement with the author(s) or other rightsholder(s); author self-archiving of the accepted manuscript version of this article is solely governed by the terms of such publishing agreement and applicable law.